


A multifield coupled thermo-chemo-mechanical theory for the reaction-diffusion modeling in photovoltaics

Zeng Liu^{1,2}  | Pietro Lenarda¹ | Jose Reinoso² | Marco Paggi¹

¹Research Unit on Multi-scale Analysis of Materials, IMT School for Advanced Studies Lucca, Lucca, Italy

²Elasticity and Strength of Materials Group, School of Engineering, University of Seville, Seville, Spain

Correspondence

Zeng Liu, IMT School for Advanced Studies Lucca, Piazza San Francesco 19, 55100, Lucca, Italy.

Email: zeng.liu@imtlucca.it

Funding information

Consejería de Economía y Conocimiento of the Junta de Andalucía, Grant/Award Number: US-1265577; H2020 Marie Skłodowska-Curie Actions, Grant/Award Number: 861061; Italian Ministry of University and Research, Grant/Award Number: 20173C478N; Spanish Ministerio de Ciencia, Innovación y Universidades, Grant/Award Number: P2-00595; Ministerio de Ciencia e Innovación of Spain, Grant/Award Number: TED2021-131649B-I00

Abstract

A comprehensive coupled thermo-chemo-mechanical modeling framework is proposed in this work to study the reaction-diffusion phenomena taking place inside photovoltaics (PV). When exposed to hygrothermal conditions, the encapsulant ethylene-co-vinyl acetate (EVA) layers undergo chemical degradation that significantly influences the overall PV performance. Aiming at efficient thermo-mechanical modeling, the coupled displacement-temperature governing equations for the EVA layers are formulated, and its 3D finite element (FE) implementation is derived in detail. Subsequently, the chemical reaction-diffusion processes occurring in the EVA layers are described, and the corresponding numerical implementation is formulated with the consideration of spatial and temporal variation of diffusivity and chemical kinetic rates. Specifically, the thermo-mechanical solution accounting for the heat generation from chemical reactions is projected to the FE model of the reaction-diffusion system in order to determine the kinetic rates and diffusion coefficients for its subsequent analysis. The proposed modeling method is applied to simulate the evolution of reaction-diffusion species at different damp heat tests, and predictions show a very satisfactory agreement with the analytical solution and experimental electroluminescence images taken from the literature. Its capabilities to predict the spatio-temporal variation are demonstrated through the simulation of the humidity freeze test, where the cyclic temperature boundary condition is imposed. With this modeling framework, it is possible to evaluate the degradation of PV modules under varying environmental boundary conditions, thus providing a guideline to design new products tailored for specific climatic zones.

KEYWORDS

finite element method, photovoltaics, reaction-diffusion, thermo-chemo-mechanical theory

1 | INTRODUCTION

Photovoltaic (PV) technology has been widely recognized as a promising solution for energy security and a low-carbon economy in the near future owing to its high efficiency and low manufacturing cost. Typical PV modules are laminates

This is an open access article under the terms of the [Creative Commons Attribution-NonCommercial](https://creativecommons.org/licenses/by-nc/4.0/) License, which permits use, distribution and reproduction in any medium, provided the original work is properly cited and is not used for commercial purposes.

© 2023 The Authors. *International Journal for Numerical Methods in Engineering* published by John Wiley & Sons Ltd.

composed of tempered glass, solar cells and encapsulant layers. The layer of silicon solar cells is used to produce electric energy, and it is protected by the tempered glass from the outdoor harsh environments.^{1–3} Despite the advantages and strengths, the PV modules are sensitive to moisture diffusion as well as chemical reactions, especially in hygrothermal outdoor environments,^{4–8} and thus its reliability is not still very competitive. A great deal of research has been focused on investigating the degradation mechanisms, see References 9–16, among many others, and most of them studied the diffusion phenomena at the constant temperature and humidity conditions. However, the realistic evaluation of PV durability is very challenging due to the coupling between the reaction-diffusion and thermo-mechanical problems and requires a multiphysics framework to comprehensively study the different failure mechanisms under changing environments.^{17–21}

Ethylene-co-vinyl acetate (EVA) is frequently used as the encapsulant material of PV modules due to its excellent physical characteristics and relatively low cost. Although the raw EVA materials are generally enhanced with chemical additives in the manufacturing process, they suffer from thermo-photo-oxidative degradation with prolonged exposure to harsh working environments.^{22–25} The typical degradation of polymer chains composing the encapsulant EVA layer involves the loss of small molecules, such as acetic acid and protons, and consequent failure at the macromolecular level. As a result, the macromolecular changes lead to the deterioration of optical properties of the EVA layers, such as browning-yellowing and snail trails.^{26,27} Besides, the permeability of the EVA layer to acidic products and moisture induces the oxidation of grid lines deposited on the surface of silicon cells, as well as adhesion and sealing degradation.^{17,28,29} Previous investigations on chemical reactions in EVA have been reported in the literature, including both experiments^{30,31} and computational modeling.^{28,32} Existing computational methods for predicting the environmental degradation of PV mainly study the diffusion under constant hygrothermal conditions and reliable models to predict the chemical reaction-diffusion under coupled thermo-mechanical loading cases are sorely lacking. Moreover, moisture and chemical species diffusion are usually dependent on temperature, and spatial variation may also exist in the presence of cracks inside the PV modules. Therefore, it is essential to establish a comprehensive thermo-chemo-mechanical modeling framework to solve the reaction-diffusion system over the 3D domain of the PV modules. This modeling method should enable the possibility to recall any realistic initial and boundary value problems and to simulate different accelerated aging tests with changing environmental loadings, such as the humidity freeze test, which could be very useful in estimating the maintenance costs and economic sustainability of PV systems.

To model the coupled problems in PV modules, a thermo-chemo-mechanical computational framework is proposed in this work, extending the pioneering approach proposed in Reference 18 to 3D problems. The dependency of reaction-diffusion on the thermo-mechanical problem is taken into account, and the governing equations are solved in a staggered manner. Analytical solutions for the diffusion proposed in Reference 28 assume constant diffusivity inside the EVA layer, and ignore the spatial variation due to temperature dependency. Although it might be feasible in steady-state temperature cases like damp heat tests, its validity cannot be ensured in varying temperature conditions. Besides, diffusion can take place not only from the free edges, but also from cracks and interspaces between solar cells, and it is almost impossible to predict these phenomena using analytical methods, as shown in Reference 33.

This work is organized as follows. In Section 2, the kinetics and constitutive formulation for the thermo-mechanical analysis are presented in detail. The chemical reaction-diffusion processes accounting for the dependency on the thermo-mechanical analysis and its mathematical description are given in Section 3. In Section 4, the weak forms and finite element implementations of the coupled thermo-chemo-mechanical governing equations are outlined. Then this computational framework is applied to simulate the reaction-diffusion phenomena occurring inside the PV modules at the international standard tests, and compared with analytical solution and electroluminescence (EL) images obtained from experimental tests, which is provided in Section 5. Finally, some concluding remarks are drawn in Section 6.

2 | THERMO-MECHANICAL FORMULATION

The formulation for the thermo-mechanical modeling of photovoltaic module with different layers (glass, silicon solar cell, backsheets, etc.) separated by EVA is described in this section. Let assume the position of each material point inside the photovoltaic module is denoted by the vector $\mathbf{x} = (x_1, x_2, x_3)^T$ in the three-dimensional Cartesian orthonormal frame $\{\mathbf{e}_1, \mathbf{e}_2, \mathbf{e}_3\}$. The temperature and displacement fields are identified by $T(x_1, x_2, x_3, t)$ and $\mathbf{u}(x_1, x_2, x_3, t)$, respectively, and T_0 is the reference temperature at the material point.

Given the infinitesimal strain tensor, the strain-displacement relation is given by

$$\boldsymbol{\varepsilon} = \frac{1}{2} (\nabla^T \mathbf{u} + \nabla \mathbf{u}), \quad (1)$$

where ∇ denotes the spatial gradient. The balance of energy in the local form reads

$$\dot{s}T_0 = Q - \nabla \cdot \mathbf{q}, \quad (2)$$

where \dot{s} stands for the entropy rate per unit volume and Q denotes the internal heat source. It should be pointed out that the small temperature change close to the reference temperature T_0 is assumed here to obtain a linear equation. In the absence of dynamic effects, the equation of motion takes the form of

$$\nabla \cdot \boldsymbol{\sigma} + \mathbf{b} = \mathbf{0}, \quad (3)$$

where $\boldsymbol{\sigma}$ is the stress tensor, and \mathbf{b} represents the body force.

According to the first and second thermodynamic laws,³⁴ the Cauchy stress tensor $\boldsymbol{\sigma}$ is conjugated to the strain tensor $\boldsymbol{\varepsilon}$, which is given by

$$\boldsymbol{\sigma} = \frac{\partial \Psi}{\partial \boldsymbol{\varepsilon}}, \quad (4)$$

where Ψ denotes the Helmholtz's free energy. Similarly, the entropy per unit volume s is thermodynamically conjugated to the temperature shift $\theta = T - T_0$,

$$s = -\frac{\partial \Psi}{\partial \theta}. \quad (5)$$

Ignoring the high-order terms in the Taylor series expansion in the vicinity of the equilibrium state ($\boldsymbol{\varepsilon} = \mathbf{0}, \theta = 0$), the Helmholtz's free energy Ψ can be obtained by

$$\Psi = \frac{1}{2} \boldsymbol{\varepsilon} : \mathbb{C} : \boldsymbol{\varepsilon} - \mathbf{z} : \boldsymbol{\varepsilon} \theta - \frac{\rho c_p}{2T_0} \theta^2, \quad (6)$$

where c_p is the specific heat capacity per unit mass, and ρ represents the density. The constitutive tensors \mathbb{C} and \mathbf{z} are defined as

$$\mathbb{C} = \frac{\partial^2 \Psi(\mathbf{0}, 0)}{\partial \boldsymbol{\varepsilon} \otimes \partial \boldsymbol{\varepsilon}}, \quad \mathbf{z} = -\frac{\partial^2 \Psi(\mathbf{0}, 0)}{\partial \boldsymbol{\varepsilon} \partial \theta}. \quad (7)$$

Note that the free energy, stress, and entropy vanish in the equilibrium ($\Psi(\mathbf{0}, 0) = 0, \boldsymbol{\sigma}(\mathbf{0}, 0) = \mathbf{0}, s(\mathbf{0}, 0) = 0$). Then the constitutive equations are given by

$$\boldsymbol{\sigma} = \frac{\partial \Psi}{\partial \boldsymbol{\varepsilon}} = \mathbb{C} : \boldsymbol{\varepsilon} - \mathbf{z} \theta, \quad (8a)$$

$$s = -\frac{\partial \Psi}{\partial \theta} = \mathbf{z} : \boldsymbol{\varepsilon} + \frac{\rho c_p}{T_0} \theta. \quad (8b)$$

According to the Fourier's law of heat conduction,^{35–37} the constitutive relation between the heat flux \mathbf{q} and the temperature shift θ can be expressed as

$$\mathbf{q} = -\mathbf{k} \cdot \nabla \theta, \quad (9)$$

where \mathbf{k} is the thermal conductivity tensor.

Assuming isotropic material behavior, the constitutive tensors are given by

$$\mathbb{C} = 2\mu \mathbb{I}^{\text{sym}} + \lambda \mathbf{1} \otimes \mathbf{1}, \quad C_{ijkl} = \mu (\delta_{ik} \delta_{jl} + \delta_{il} \delta_{jk}) + \lambda \delta_{ij} \delta_{kl}, \quad (10a)$$

$$\mathbf{z} = \alpha(3\lambda + 2\mu)\mathbf{1}, \quad z_{ij} = \alpha(3\lambda + 2\mu)\delta_{ij}, \quad (10b)$$

$$\mathbf{k} = \kappa \mathbf{1}, \quad k_{ij} = \kappa \delta_{ij}, \quad (10c)$$

where λ and μ are Lamé constants, α is the thermal expansion coefficient, κ is the thermal conductivity, $\mathbf{1}$ is the second-order identity tensor, and \mathbb{I}^{sym} is the fourth-order symmetric identity tensor.

3 | CHEMICAL REACTION-DIFFUSION PROCESSES AND THE MATHEMATICAL DESCRIPTION

Chemical degradation of polymeric materials takes place in three different pathways, including chain scission, no significant molecular change, and crosslinking,³⁸ and these reactions occurring in polymers can be described by first-order kinetic equations.³⁹ Note that the crosslinking can be neglected since the raw EVA copolymer materials are cured resins with much more crosslinking than that generated during the reaction process.⁴⁰ In the following, each chemical specie is assumed to be distinguishable within a class, such as radicals and unsaturated or carbonyl compounds. For convenience, each chemical specie is denoted with a capital letter (e.g., U , C_b , and VAc), and the corresponding molar concentration of characteristic bonds are denoted by capital letters with brackets (e.g., $[U]$, $[C_b]$, and $[VAc]$).

In the cases where the molecular weight does not significantly vary with time, reactions include only the loss of radicals or small molecules that diffuse through the polymeric layers. Generally, the transformation of the macromolecular chain can be expressed as



where P is the native molecule, P^* denotes the degraded molecule, and S represents the small molecules produced during the chemical reaction processes. Assuming k is the rate of reaction, the rate of the concentration change for the two chemical species P and P^* can be defined as

$$-\frac{d[P]}{dt} = \frac{d[P^*]}{dt} = k[P], \quad (12)$$

where concentrations of P and P^* are functions of the extent of chemical reactions, and its rate k depends on temperature according to the Arrhenius law^{41,42}

$$k = A_0 \exp\left(-\frac{E_a}{RT}\right), \quad (13)$$

where $R = 8.314 \text{ J/(K mol)}$ is the ideal gas constant, E_a is the activation energy, and A_0 denotes the pre-exponential coefficient. On the other hand, when the chain scission phenomenon occurs, the number of molecules changes along the chemical reaction process, which can be expressed as



where P' and P'' are the different chemical species involved in this process. The generation rates of P' and P'' are equivalent to the consumption rate of P , which takes the form of

$$-\frac{d[P]}{dt} = \frac{d[P']}{dt} = \frac{d[P'']}{dt} = k[P]. \quad (15)$$

With regard to the degradation of EVA composed of ethylene (ET) and vinyl acetate (VAc), a lot of experimental studies for the explanation of the involved chemical reactions were reported, see References 43 and 30. Given the photo-oxidative degradation of EVA,²⁶ the comprehensive degradation is depicted in Figure 1, and the nomenclature of chemical species is summarized in Table 1. Both ET and VAc undergo different chemical degradation processes,¹⁸ which are triggered by temperature and the presence of oxygen and moisture. From Figure 1, it can be seen that the linear portions of EVA involve H abstraction (Reactions 1 and 2), oxidation (Reaction 3), and loss of acetate units (Reactions 4 and 5). ET units are chemically inert species due to the small dipole moment related to the C—H bonds, but the copolymerization with VAc increases the reactivity. The C—H and C—C bonds inside ET units do not absorb the radiation, and the initiation of photo-oxidation requires the existence of chromophores like carbonyl groups and stabilizers.⁴⁴ The initial degradation of

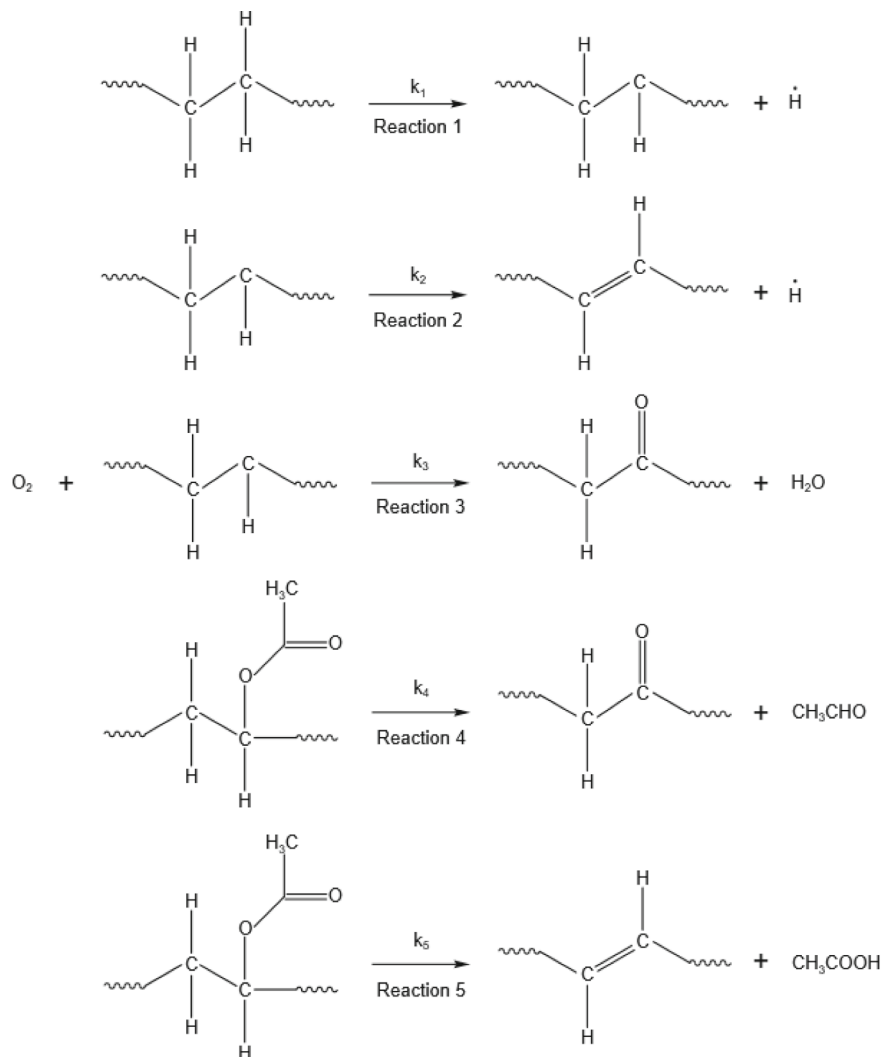


FIGURE 1 Chemical reactions involving the EVA macromolecules.

ET is the generation of radical species, see Reaction 1 in Figure 1. The loss of atomic hydrogen leads to the formation of radicals and unpaired radicals in the backbone or a terminal position after the chain cleavage, which usually occurs in molten polymers. The formed radical H^\bullet after the cleavage of the C—H bond diffuses towards noncrystalline areas and reacts with other radical species in EVA. This initial reaction process can be expressed as

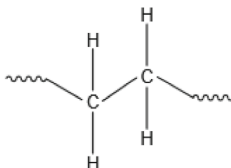
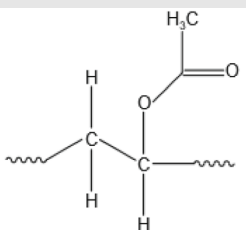
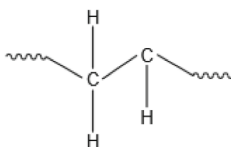
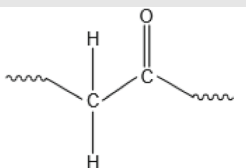
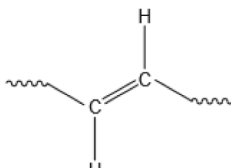


Note that the formed radical specie R^\bullet does not diffuse inside the EVA layers since it is formed in the polymer backbone.

After the first chemical reaction, further degradation occurs through two different mechanisms in the presence of the formed radical in the backbone and free H^\bullet . The first mechanism is that H^\bullet can abstract another H^\bullet close to the unpaired C radical due to the high reactivity of the radical site in the backbone, which produces H_2 molecules and the unsaturated bonds in accordance with the Norrish Type I reaction,⁴⁵ see Reaction 2 in Figure 1. Another degradation scheme involves the presence of absorbed oxygen from the environment, causing the formation of water molecules and carbonyl groups in the backbone,⁴⁶ see Reaction 3 in Figure 1. The Reactions 2 and 3 are given by



TABLE 1 Chemical species, nomenclature, and definition in the reaction-diffusion processes.

Chemical structure	Nomenclature	Definition
	<i>ET</i>	Ethylene units
	<i>VAc</i>	Vinyl acetate units
	<i>R</i> [•]	Radical with one electron
	<i>C_b</i>	Carbonyl bond C=O
	<i>U</i>	C=C bond

where $U^{(R2)}$ and $C_b^{(R3)}$ represent the formed double-bonds and the carbonyl groups in the Reactions 2 and 3, respectively. It is worth noting that the molecules H^{\bullet} and H_2O can diffuse in the EVA while double-bonds and the carbonyl groups in the backbone do not diffuse.

The *VAc* portions also show two different mechanisms through the loss of acetate units, as reported in Reference 47. Reactions lead to the formation of acetaldehyde through the Norrish type I mechanism (see Reaction 4 in Figure 1) and acetic acid through the type II mechanism (see Reaction 5 in Figure 1). These two reactions can be schematized as



where $U^{(R5)}$ and $C_b^{(R4)}$ denote the formed unsaturations and carbonyl groups in the reactions, while CH_3CHO and CH_3COOH are the small molecules that can diffuse in the EVA layers.

Generally, the involved chemical degradation mechanisms can be described by the following reaction systems¹⁸

$$\frac{d[ET]}{dt} = -k_1[ET], \quad (19a)$$

$$\frac{d[VAc]}{dt} = -(k_4 + k_5)[VAc], \quad (19b)$$

$$\frac{d[R^*]}{dt} = k_1[ET] - k_2[R^*] - k_3[R^*][O_2], \quad (19c)$$

$$\frac{d[U]}{dt} = k_2[R^*] + k_5[VAc], \quad (19d)$$

$$\frac{d[C_b]}{dt} = k_3[R^*][O_2] + k_4[VAc], \quad (19e)$$

where the starting species ET and VAc , the intermediate specie R^* , and other products U and C_b are the unknown variables of the chemical reaction system. For simplicity, the following concentration vector of the chemical species is introduced

$$\mathbf{C}(t) = ([ET], [VAc], [R^*], [U], [C_b])^T. \quad (20)$$

Thus the previous differential equations of the reaction system can be written in vectorial form, which is given by

$$\frac{\partial \mathbf{C}(t)}{\partial t} - \mathbf{K}(\theta)\mathbf{C}(t) = \mathbf{0}, \quad \text{in } \Omega \times [0, t_f], \quad (21)$$

where $\mathbf{K}(\theta)$ is the temperature-dependent matrix, and Ω is the domain of the EVA layer. The boundary conditions of the chemical reaction system can be defined as

$$\mathbf{C}(t) = \mathbf{C}^*(t), \quad \text{in } \Omega \times [0, t_f]. \quad (22)$$

Regarding the diffusion systems involved in the degradation of EVA, the moisture and oxygen diffusion is taken into account and can be described by the following partial differential equations

$$\frac{\partial [O_2]}{\partial t} - D_1 \Delta [O_2] = -k_3 [R^*][O_2], \quad (23a)$$

$$\frac{\partial [H_2O]}{\partial t} - D_2 \Delta [H_2O] = k_3 [R^*][O_2], \quad (23b)$$

where D_1 and D_2 are temperature dependent diffusion coefficients, which are given by

$$D_j(T) = \begin{cases} D_j^0 \exp\left(-\frac{E_j^d}{RT}\right), & \text{if } \Delta_n \leq \delta_n^c, \\ D_j^0 \exp\left(-\frac{E_j^d}{RT}\right) \frac{\Delta_n}{\delta_n^c}, & \text{if } \Delta_n > \delta_n^c, \end{cases} \quad (24)$$

where D_j^0 ($j = 1, 2$) are the coefficients for the limit cases of vanishing concentration that are assumed to be linear increasing functions of the interfacial gap Δ_n when it overcomes the critical value δ_n^c , and E_j^d ($j = 1, 2$) denotes the activation energy of diffusion.⁴⁸

Let define the diffusion specie concentration as $c(\mathbf{x}, t)$ representing $[H_2O]$ or $[O_2]$, and the partial differential equation for the diffusion in EVA can be rewritten in the vectorial form as

$$\frac{\partial c(\mathbf{x}, t)}{\partial t} - D(T)\Delta c(\mathbf{x}, t) = r, \quad \text{in } \Omega \times [0, t_f], \quad (25)$$

where $D(T)$ is the corresponding diffusion coefficient, and r is related to the right-hand side terms in Equation (23a,b). The initial and Dirichlet boundary conditions for the diffusion system are given by

$$c(\mathbf{x}, 0) = 0, \quad \text{in } \Omega \times [0, t_f], \quad (26a)$$

$$c(\mathbf{x}, t) = c^*(\mathbf{x}, t), \quad \text{in } \partial\Omega \times [0, t_f], \quad (26b)$$

where $c^*(\mathbf{x}, t)$ denotes the imposed Dirichlet boundary condition.

The internal heat Q generated by chemical reactions can be defined as

$$Q = Q_{ET} + Q_{VAc} + Q_{R^\bullet}, \quad (27)$$

with

$$Q_{ET} = \Delta H_{R1} k_1 [ET], \quad (28a)$$

$$Q_{R^\bullet} = (\Delta H_{R2} k_2 + \Delta H_{R3} k_3) [R^\bullet], \quad (28b)$$

$$Q_{VAc} = (\Delta H_{R4} k_4 + \Delta H_{R5} k_5) [VAc]. \quad (28c)$$

4 | COMPUTATIONAL SCHEMES AND FINITE ELEMENT INTERPOLATION

In this section, the weak forms of the thermo-mechanical boundary value problems, as well as the reaction-diffusion system will be derived for the finite element implementation. In order to advance the solution within a time increment, let assume the finite time increment (t_n, t_{n+1}) , where $\Delta t = t_{n+1} - t_n$ denotes the increment length.⁴⁹ As a result, the strain rate vector $\dot{\mathbf{e}}$, temperature rate $\dot{\theta}$, and the rate of diffusion specie \dot{c} are all considered to be constant in the time increment and defined by

$$\dot{\mathbf{e}} = \frac{\mathbf{e}_{n+1} - \mathbf{e}_n}{\Delta t}, \quad \dot{\theta} = \frac{\theta_{n+1} - \theta_n}{\Delta t}, \quad \dot{c} = \frac{c_{n+1} - c_n}{\Delta t}. \quad (29)$$

Note that due to the given values \mathbf{e}_n , θ_n , and c_n at time t_n , the above rates associated with time increment Δt are linear functions of \mathbf{e}_{n+1} , θ_{n+1} , and c_{n+1} at time t_{n+1} .

4.1 | Implementation of the thermo-mechanical formulation

Let assume the solid body at thermodynamic equilibrium, described by the independent variables (\mathbf{u}, θ) and identified with the closed domain Ω . The weak form of Equation (2) can be obtained by multiplying it with a test function $\delta\theta$ and integrating over the whole domain Ω of the body, which takes the form of

$$\int_{\Omega} (T_0 \dot{s} + \nabla \cdot \mathbf{q} - Q) \delta\theta \, d\Omega = 0. \quad (30)$$

Recalling Equation (8b) and by the use of divergence theorem, the weak form of Equation (30) can be reformulated as

$$\int_{\Omega} (T_0 \mathbf{z} : \dot{\boldsymbol{\varepsilon}} + \rho c_p \dot{\theta} - Q) \delta\theta \, d\Omega - \int_{\Omega} \mathbf{q} \cdot \nabla \delta\theta \, d\Omega + \int_{\partial\Omega_{\bar{q}}} \mathbf{q} \cdot \mathbf{n} \delta\theta \, d\Omega = 0. \quad (31)$$

The analogous procedure can be applied to Equation (3), by multiplying it with a test function $\delta\mathbf{u}$ and integrating over the whole domain Ω , and the weak form in the absence of body force is given by

$$- \int_{\Omega} \boldsymbol{\sigma} : \delta\boldsymbol{\varepsilon} \, d\Omega + \int_{\partial\Omega_{\bar{\boldsymbol{\tau}}}} \boldsymbol{\sigma} \cdot \mathbf{n} \cdot \delta\mathbf{u} \, d\Omega = 0. \quad (32)$$

Appropriate boundary conditions must be specified so that the thermo-mechanical boundary value problem is well-posed and the obtained solution is unique. The mixed mechanical boundary conditions are defined on $\partial\Omega = \partial\Omega_{\bar{\boldsymbol{\tau}}} \cup \partial\Omega_{\bar{\mathbf{u}}}$ and the mixed thermal boundary conditions are defined on $\partial\Omega = \partial\Omega_{\bar{\theta}} \cup \partial\Omega_{\bar{q}}$, which can be expressed as

$$\begin{aligned} \boldsymbol{\sigma} \cdot \mathbf{n} &= \bar{\boldsymbol{\tau}}_n \text{ on } \partial\Omega_{\bar{\boldsymbol{\tau}}}, & \mathbf{u} &= \bar{\mathbf{u}} \text{ on } \partial\Omega_{\bar{\mathbf{u}}}, \\ \mathbf{q} \cdot \mathbf{n} &= \bar{q}_n \text{ on } \partial\Omega_{\bar{q}}, & \theta &= \bar{\theta} \text{ on } \partial\Omega_{\bar{\theta}}. \end{aligned} \quad (33)$$

According to the finite element method, the domain Ω for the thermo-mechanical problem can be discretized into n_e nonoverlapping finite elements, that is, $\Omega \approx \bigcup_{e=1}^{n_e} \Omega_e$. Based on the isoparametric interpolation, the approximate position vector \mathbf{x} at any material point inside the corresponding finite element can be calculated by interpolating the nodal values through shape functions as follows

$$\mathbf{x} \approx \sum_{I=1}^{n_n} \mathbf{N}_I(\xi) \mathbf{x}_I = \mathbf{N} \tilde{\mathbf{x}}, \quad (34)$$

where \mathbf{x}_I is the nodal position vector in the element level with the number of nodes $n_n = 8$, and \mathbf{N}_I is the shape function, which is defined as

$$\mathbf{N}_I = \begin{bmatrix} N_I & 0 & 0 \\ 0 & N_I & 0 \\ 0 & 0 & N_I \end{bmatrix}, \quad (35)$$

where $N_I = \frac{1}{8} (1 + \xi_I^1 \xi^1) (1 + \xi_I^2 \xi^2) (1 + \xi_I^3 \xi^3)$, $I = 1, 2, \dots, 8$. The displacement and temperature fields (\mathbf{u}, θ) , the variations $(\delta \mathbf{u}, \delta \theta)$, and the increments $(\Delta \mathbf{u}, \Delta \theta)$, are approximated by

$$\mathbf{u} \approx \sum_{I=1}^{n_n} \mathbf{N}_I(\xi) \mathbf{d}_I = \mathbf{N} \mathbf{d}, \quad \delta \mathbf{u} \approx \sum_{I=1}^{n_n} \mathbf{N}_I(\xi) \delta \mathbf{d}_I = \mathbf{N} \delta \mathbf{d}, \quad \Delta \mathbf{u} \approx \sum_{I=1}^{n_n} \mathbf{N}_I(\xi) \Delta \mathbf{d}_I = \mathbf{N} \Delta \mathbf{d}, \quad (36a)$$

$$\theta \approx \sum_{I=1}^{n_n} N_I(\xi) \theta_I = \hat{\mathbf{N}} \theta, \quad \delta \theta \approx \sum_{I=1}^{n_n} N_I(\xi) \delta \theta_I = \hat{\mathbf{N}} \delta \theta, \quad \Delta \theta \approx \sum_{I=1}^{n_n} N_I(\xi) \Delta \theta_I = \hat{\mathbf{N}} \Delta \theta, \quad (36b)$$

where \mathbf{d}_I and θ_I represent the nodal displacement and temperature shift, respectively, and \mathbf{d} and θ correspond to the vectors in the element level.

The strain field in the vectorial form can be expressed as $\mathbf{e} = [\varepsilon_{11}, \varepsilon_{22}, \varepsilon_{33}, 2\varepsilon_{12}, 2\varepsilon_{13}, 2\varepsilon_{23}]^T$. Its interpolation, the variation $\delta \mathbf{e}$, and the increment $\Delta \mathbf{e}$ are approximated by

$$\mathbf{e} \approx \sum_{I=1}^{n_n} \mathbf{B}_I(\xi) \mathbf{d}_I = \mathbf{B} \mathbf{d}, \quad \delta \mathbf{e} \approx \sum_{I=1}^{n_n} \mathbf{B}_I(\xi) \delta \mathbf{d}_I = \mathbf{B} \delta \mathbf{d}, \quad \Delta \mathbf{e} \approx \sum_{I=1}^{n_n} \mathbf{B}_I(\xi) \Delta \mathbf{d}_I = \mathbf{B} \Delta \mathbf{d}, \quad (37)$$

where \mathbf{B}_I is the strain interpolation matrix that can be expressed as

$$\mathbf{B}_I = \begin{bmatrix} \frac{\partial N_I}{\partial x_1} & 0 & 0 \\ 0 & \frac{\partial N_I}{\partial x_2} & 0 \\ 0 & 0 & \frac{\partial N_I}{\partial x_3} \\ \frac{\partial N_I}{\partial x_2} & \frac{\partial N_I}{\partial x_1} & 0 \\ \frac{\partial N_I}{\partial x_3} & 0 & \frac{\partial N_I}{\partial x_1} \\ 0 & \frac{\partial N_I}{\partial x_3} & \frac{\partial N_I}{\partial x_2} \end{bmatrix}. \quad (38)$$

Similarly, the interpolations of the temperature gradient $\nabla \theta$, its variation $\nabla \delta \theta$, and its increment $\nabla \Delta \theta$ read

$$\nabla \theta \approx \sum_{I=1}^{n_n} \mathbf{B}_I^\theta(\xi) \theta_I = \mathbf{B}^\theta \theta, \quad \nabla \delta \theta \approx \sum_{I=1}^{n_n} \mathbf{B}_I^\theta(\xi) \delta \theta_I = \mathbf{B}^\theta \delta \theta, \quad \nabla \Delta \theta \approx \sum_{I=1}^{n_n} \mathbf{B}_I^\theta(\xi) \Delta \theta_I = \mathbf{B}^\theta \Delta \theta, \quad (39)$$

where \mathbf{B}_I^θ is the corresponding gradient interpolation matrix, which is given by

$$\mathbf{B}_I^\theta = \begin{bmatrix} \frac{\partial N_I}{\partial x_1} & \frac{\partial N_I}{\partial x_2} & \frac{\partial N_I}{\partial x_3} \end{bmatrix}^T. \quad (40)$$

Inserting the interpolation formulae into Equation (31), the discrete form of energy balance is given by

$$\hat{\mathcal{R}}_{\text{int}}^{\theta}(\mathbf{d}, \theta, \delta\theta) = \delta\theta^T \left[\int_{\Omega} \hat{\mathbf{N}}^T (\rho c_p \dot{\theta} + T_0 \mathbf{Z}^T \dot{\mathbf{e}} - Q) \, d\Omega + \int_{\Omega} (\mathbf{B}^{\theta})^T \kappa \nabla \theta \, d\Omega + \int_{\partial\Omega_{\bar{q}}} \hat{\mathbf{N}}^T \bar{q}_n \, d\partial\Omega \right], \quad (41)$$

where \mathbf{Z} is the constitutive vector and expressed as

$$\mathbf{Z} = \begin{bmatrix} \alpha(3\lambda + 2\mu) & \alpha(3\lambda + 2\mu) & \alpha(3\lambda + 2\mu) & 0 & 0 & 0 \end{bmatrix}^T. \quad (42)$$

Besides, the discrete form of motion balance can be expressed as

$$\hat{\mathcal{R}}_{\text{int}}^u(\mathbf{d}, \theta, \delta\mathbf{d}) = \delta\mathbf{d}^T \left[\int_{\Omega} \mathbf{B}^T \mathbf{s} \, d\Omega + \int_{\partial\Omega_{\bar{\mathbf{t}}}} \mathbf{N}^T \bar{\mathbf{t}}_n \, d\partial\Omega \right], \quad (43)$$

where \mathbf{s} is the stress field in the vectorial form that is given by $\mathbf{s} = [\sigma_{11}, \sigma_{22}, \sigma_{33}, \sigma_{12}, \sigma_{13}, \sigma_{23}]^T$.

By ignoring the heat flux and traction terms, the residual internal vectors associated with the energy and motion balances are given by

$$\mathbf{R}_{\text{int}}^{\theta}(\mathbf{d}, \theta) = \int_{\Omega} \hat{\mathbf{N}}^T (\rho c_p \dot{\theta} + T_0 \mathbf{Z}^T \dot{\mathbf{e}} - Q) \, d\Omega + \int_{\Omega} (\mathbf{B}^{\theta})^T \kappa \nabla \theta \, d\Omega, \quad (44a)$$

$$\mathbf{R}_{\text{int}}^d(\mathbf{d}, \theta) = \int_{\Omega} \mathbf{B}^T \mathbf{s} \, d\Omega. \quad (44b)$$

An iterative scheme is adopted for the solution of the coupled nonlinear thermo-mechanical residual equations, and the consistent linearization can be expressed as

$$\begin{bmatrix} \mathbf{k}_{dd} & \mathbf{k}_{d\theta} \\ \mathbf{k}_{\theta d} & \mathbf{k}_{\theta\theta} \end{bmatrix} \begin{bmatrix} \Delta\mathbf{d} \\ \Delta\theta \end{bmatrix} = - \begin{bmatrix} \mathbf{R}_{\text{int}}^d \\ \mathbf{R}_{\text{int}}^{\theta} \end{bmatrix}, \quad (45)$$

where \mathbf{k}_{ab} with $\{a, b\} = \{d, \theta\}$ are different tangent operators, and given by

$$\mathbf{k}_{\theta\theta} = \int_{\Omega} \left(-\frac{\rho c_p}{\Delta t} + \frac{\partial Q}{\partial \theta} \right) \hat{\mathbf{N}}^T \hat{\mathbf{N}} \, d\Omega - \int_{\Omega} \kappa (\mathbf{B}^{\theta})^T \mathbf{B}^{\theta} \, d\Omega, \quad (46a)$$

$$\mathbf{k}_{\theta d} = - \int_{\Omega} \frac{T_0}{\Delta t} \hat{\mathbf{N}}^T \mathbf{Z}^T \mathbf{B} \, d\Omega, \quad (46b)$$

$$\mathbf{k}_{d\theta} = - \int_{\Omega} \mathbf{B}^T \mathbf{Z} \hat{\mathbf{N}} \, d\Omega, \quad (46c)$$

$$\mathbf{k}_{dd} = - \int_{\Omega} \mathbf{B}^T \mathbb{C} \mathbf{B} \, d\Omega, \quad (46d)$$

where \mathbb{C} represents the elastic stiffness matrix.

4.2 | Implementation of the reaction-diffusion system

In the sequel, the weak forms and finite element implementation of the reaction-diffusion system will be derived in detail. By multiplying the differential systems Equation (25) with a test function δc and integrating over the whole domain using the divergence theorem, the weak form of the system can be constructed as

$$\int_{\Omega} \frac{\partial c}{\partial t} \delta c \, d\Omega + \int_{\Omega} D \nabla c \cdot \nabla \delta c \, d\Omega = \int_{\Omega} r \delta c \, d\Omega. \quad (47)$$

The finite element interpolation of the diffusion specie vector c and its variation δc in a general material point can be obtained through the linear Lagrange shape functions

$$c \approx \sum_{I=1}^{n_n} N_I(\xi) c_I = \mathbf{N}_c \tilde{\mathbf{c}}, \quad \delta c \approx \sum_{I=1}^{n_n} N_I(\xi) \delta c_I = \mathbf{N}_c \delta \tilde{\mathbf{c}}, \quad (48)$$

where $\tilde{\mathbf{c}}$ is the nodal vector of diffusion specie at the element level.

Besides, the finite element interpolation of the spatial gradient of diffusion specie ∇c and its variation $\nabla \delta c$ in the vectorial form can be determined as

$$\nabla c \approx \sum_{I=1}^{n_n} \mathbf{B}_{c,I} c_I = \mathbf{B}_c \tilde{\mathbf{c}}, \quad \nabla \delta c \approx \sum_{I=1}^{n_n} \mathbf{B}_{c,I} \delta c_I = \mathbf{B}_c \delta \tilde{\mathbf{c}}, \quad (49)$$

where the interpolation matrix $\mathbf{B}_{c,I}$ is defined as

$$\mathbf{B}_{c,I} = \begin{bmatrix} \frac{\partial N_I}{\partial x_1} & 0 & 0 \\ 0 & \frac{\partial N_I}{\partial x_2} & 0 \\ 0 & 0 & \frac{\partial N_I}{\partial x_3} \end{bmatrix}. \quad (50)$$

Introducing Equation (48) and Equation (49) into Equation (47), the discrete form of the reaction-diffusion system can be obtained as

$$\delta \tilde{\mathbf{c}}^T \int_{\Omega} (D \mathbf{B}_c^T \mathbf{B}_c \tilde{\mathbf{c}} + \mathbf{N}_c^T \dot{c} - \mathbf{N}_c^T r) \, d\Omega = \delta \tilde{\mathbf{c}}^T \mathbf{f}_{\text{int}}^c, \quad (51)$$

where $\mathbf{f}_{\text{int}}^c$ is the internal residual vector of the reaction-diffusion system, which is expressed as

$$\mathbf{f}_{\text{int}}^c = \int_{\Omega} (D \mathbf{B}_c^T \mathbf{B}_c \tilde{\mathbf{c}} + \mathbf{N}_c^T \dot{c} - \mathbf{N}_c^T r) \, d\Omega. \quad (52)$$

To solve the nonlinear residual equations with regard to the diffusion system, an iterative Newton–Raphson scheme is adopted, and the consistent linearization reads

$$\mathbf{K}^c \Delta \tilde{\mathbf{c}} = -\mathbf{f}_{\text{int}}^c, \quad (53)$$

where \mathbf{K}^c is the stiffness for the diffusion system and takes the form of

$$\mathbf{K}^c = \int_{\Omega} \left(-D \mathbf{B}_c^T \mathbf{B}_c - \frac{1}{\Delta t} \mathbf{N}_c^T \mathbf{N}_c + \frac{\partial r}{\partial c} \mathbf{N}_c^T \mathbf{N}_c \right) \, d\Omega. \quad (54)$$

4.3 | Algorithms for the coupled theory

To address the multifield coupled thermo-chemo-mechanical problem with application to photovoltaics, the staggered scheme is exploited to solve the discrete equations that describe the whole process. Specifically, the thermo-mechanical problem is firstly solved through the fully implicit scheme, and subsequently, the reaction-diffusion is addressed with the consideration of spatio-temporal variation of deformation and temperature.

Let assume t_n and $t_{n+1}^{(k+1)}$ denote the previous converged increment and prospective current increment at iteration $k+1$, respectively. In the thermo-mechanical analysis, given the data $\{\mathbf{d}_n, \boldsymbol{\theta}_n, \mathbf{C}_n\}$ at the previous time increment, the following linearized system needs to be solved through the Newton–Raphson scheme

$$\begin{bmatrix} \mathbf{k}_{dd,n+1}^{(k)} & \mathbf{k}_{d\theta,n+1}^{(k)} \\ \mathbf{k}_{\theta d,n+1}^{(k)} & \mathbf{k}_{\theta\theta,n+1}^{(k)} \end{bmatrix} \begin{bmatrix} \Delta \mathbf{d}_{n+1}^{(k+1)} \\ \Delta \boldsymbol{\theta}_{n+1}^{(k+1)} \end{bmatrix} = - \begin{bmatrix} \mathbf{R}_{\text{int},n+1}^{d(k)} \\ \mathbf{R}_{\text{int},n+1}^{\theta(k)} \end{bmatrix} \quad (55)$$

so that the updated $\{\mathbf{d}_{n+1}^{(k+1)}, \boldsymbol{\theta}_{n+1}^{(k+1)}\}$ can be obtained by

$$\begin{cases} \mathbf{d}_{n+1}^{(k+1)} = \mathbf{d}_{n+1}^{(k)} + \Delta \mathbf{d}_{n+1}^{(k+1)} \\ \boldsymbol{\theta}_{n+1}^{(k+1)} = \boldsymbol{\theta}_{n+1}^{(k)} + \Delta \boldsymbol{\theta}_{n+1}^{(k+1)} \end{cases} \quad (56)$$

This procedure is repeated until both the largest residual norm and the largest correction to the solution are less than the prescribed tolerance values. The numerical implementation procedure of thermo-mechanical formulation is summarized in Algorithm 1.

Algorithm 1. Numerical implementation algorithm of the thermo-mechanical formulation

Data: $\mathbf{d}_n, \theta_n, \mathbf{C}_n$

Result: $\mathbf{d}_{n+1}, \theta_{n+1}$

while $\|\mathbf{R}\| > \textit{tolerance}$ **do**

for $n \leftarrow 1$ **to** 8 integration points **do**

 Compute the shape function matrix $\mathbf{N}_{n+1}^{(k)}$ and $\hat{\mathbf{N}}_{n+1}^{(k)}$ Compute the strain interpolation matrix $\mathbf{B}_{n+1}^{(k)}$ Compute the temperature gradient interpolation matrix $\mathbf{B}_{n+1}^{\theta(k)}$ Compute the constitutive matrices $\mathbf{Z}_{n+1}^{(k)}$ and $\mathbf{C}_{n+1}^{(k)}$ Compute the internal heat generated by chemical reactions $Q_{n+1}^{(k)}$

 Compute the stiffness matrices $\mathbf{k}_{dd,n+1}^{(k)}, \mathbf{k}_{d\theta,n+1}^{(k)}, \mathbf{k}_{\theta d,n+1}^{(k)}$ and $\mathbf{k}_{\theta\theta,n+1}^{(k)}$ Compute the internal force vectors $\mathbf{R}_{int,n+1}^{d(k)}$ and $\mathbf{R}_{int,n+1}^{\theta(k)}$ Update the solution variables $\mathbf{d}_{n+1}^{(k+1)}$ and $\boldsymbol{\theta}_{n+1}^{(k+1)}$ by Equation (56)

The iterative scheme is also applied to the solution of discrete equations corresponding to diffusion, and the linearized system can be expressed as

$$\mathbf{K}_{n+1}^{c(k)} \Delta \tilde{\mathbf{c}}_{n+1}^{(k+1)} = -\mathbf{f}_{int,n+1}^{c(k)} \quad (57)$$

where the tangent operator $\mathbf{K}_{n+1}^{c(k)}$ are determined by the thermo-mechanical solution. Given the solution of Equation (57), the updated approximation for $\tilde{\mathbf{c}}_{n+1}^{(k+1)}$ can be obtained as $\tilde{\mathbf{c}}_{n+1}^{(k+1)} = \tilde{\mathbf{c}}_{n+1}^{(k)} + \Delta \tilde{\mathbf{c}}_{n+1}^{(k+1)}$. The iteration ends when both the largest residual and the largest correction to the solution are less than the prescribed tolerance values.

Regarding the solution of reaction ordinary differential equations Equation (21), an implicit time integration scheme is adopted, and the set of algebraic equations at each time increment is given by

$$\frac{1}{\Delta t} (\mathbf{C}_{n+1} - \mathbf{C}_n) - \mathbf{K}_{n+1}^r \mathbf{C}_{n+1} = \mathbf{0}, \quad (58)$$

where \mathbf{C}_{n+1} and \mathbf{C}_n are the reaction concentration vectors at the current and previous time increments, respectively. Note that \mathbf{K}_{n+1}^r is determined from the temperature field obtained by solving the thermo-mechanical problem using the finite element discretization. The proposed implementation algorithm for the chemical reaction-diffusion system is summarized in Algorithm 2.

5 | NUMERICAL EXAMPLES AND VALIDATION

In this section, two different accelerated ageing cases with and without temperature variation are simulated to demonstrate the capability of the proposed thermo-chemo-mechanical computational framework. The first ageing case is the damp heat test with constant moisture and temperature condition, and thus the mass diffusion and chemical reactions can be decoupled from the thermo-mechanical problem, allowing the comparison of numerical prediction with analytical solution and available experimental EL images for validation purposes. The second case is the humidity freeze test with the cyclic hygrothermal condition, which requires the fully coupled modeling framework since the reaction-diffusion phenomena occurring in EVA depend on the solution obtained from the thermo-mechanical analysis.

Algorithm 2. Numerical implementation algorithm of the reaction-diffusion formulation**Data:** $\tilde{\mathbf{c}}_n, \mathbf{C}_n, \mathbf{d}_{n+1}, \theta_{n+1}$ **Result:** $\tilde{\mathbf{c}}_{n+1}, \mathbf{C}_{n+1}$ **while** $\|\mathbf{R}\| > \textit{tolerance}$ **do** **for** $n \leftarrow 1$ **to** 8 *integration points* **do** Compute the shape function matrix $\mathbf{N}_{c,n+1}^{(k)}$ Compute the gradient interpolation matrix $\mathbf{B}_{c,n+1}^{(k)}$ Compute the temperature $T_{n+1}^{(k)}$ with θ_{n+1} obtained from Algorithm 1 Compute the normal gap at the integration point Δ_n with \mathbf{d}_{n+1} **if** $\Delta_n \leq \delta_n^c$ **then** Compute the coefficient $D_{j,n+1}^{(k)} = D_j^0 \exp\left(-\frac{E_j^d}{RT_{n+1}^{(k)}}\right)$ **else** **end** Compute the coefficient $D_{j,n+1}^{(k)} = D_j^0 \exp\left(-\frac{E_j^d}{RT_{n+1}^{(k)}}\right) \frac{\Delta_n}{\delta_n^c}$ Compute the stiffness matrix of chemical reactions \mathbf{K}_{n+1}^r Update the concentration vector of chemical reactions \mathbf{C}_{n+1} **end** Compute the stiffness matrices of diffusion $\mathbf{K}_{n+1}^{c(k)}$ Compute the internal force vectors of diffusion $\mathbf{f}_{int,n+1}^{c(k)}$ Update the solution variables $\tilde{\mathbf{c}}_{n+1}^{(k+1)}$ by Equation (57)**end****FIGURE 2** The sketch of double-glass structure in the damp heat test.**5.1 | Damp heat test**

To simulate the damp heat test, a double glass laminate with an EVA layer encapsulated by two glass plates is considered, see the schematic diagram in Figure 2. The thickness of the glass is 3 mm, while the thickness of EVA is 0.5 mm. In this structure, the only path allowable for diffusion is the side areas between the two glass plates and edge-sealing materials to fill the gap are not considered in line with the experimental work.⁵⁰ According to Reference 51, the analytical solution of spatial and temporal concentration can be obtained by

$$c = c^* + \frac{4c^*}{\pi} \sum_{m=0}^{\infty} \frac{1}{2m+1} \sin\left[\frac{(2m+1)\pi x}{l}\right] \exp[-D(2m+1)^2 \pi^2 t/l^2], \quad (59)$$

where c^* denotes the boundary concentration, x represents the distance from the edge, and l stands for the width of the module. The comparison between the spatial variation of moisture concentration obtained from the diffusion model and analytical method is shown in Figure 3, and as clearly seen, they agree with each other very well for the two different boundary concentration values corresponding to the average conditions in Miami.²⁸ A series of damp heat tests were also examined with the double glass modules exposed to four different hot and humid conditions, namely 85°C/85% RH, 65°C/85% RH, 45°C/85% RH, and 85°C/40% RH, which correspond to the absolute humidity of 2.74, 1.25, 0.508, and 1.29 kg/cm³, respectively.⁵⁰ Model parameters corresponding to the chemical reactions are listed in Table 2. The initial concentrations of the chemical species over the whole volume are prescribed as $\mathbf{C}_{init} = (0.64, 0.32, 0, 0, 0)^T$ with the unit of mol/m³. To avoid possible numerical instability,⁵² the mesh size of the finite element model is set to 3 mm, and the total number of elements for the EVA layer is 2860.

The contour plots of moisture diffusion in the 85°C/85% RH damp heat test obtained from simulation are shown in Figure 4 and compared with the corresponding experimental EL images at different time points.⁵⁰ As can be seen

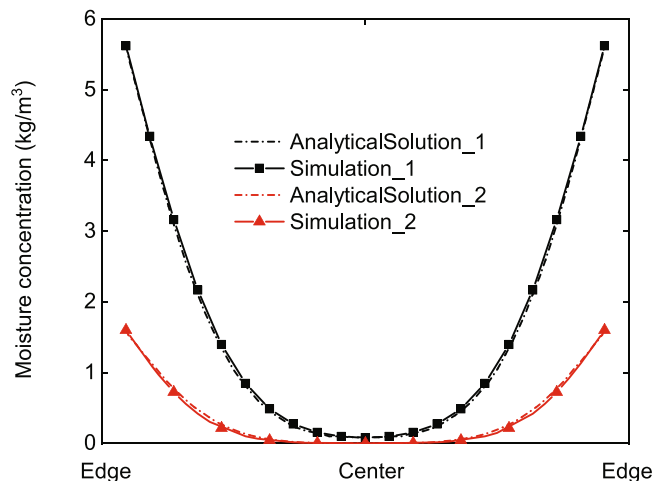


FIGURE 3 The comparison of predicted moisture distribution across the EVA layer between the analytical solutions²⁸ and numerical predictions.

TABLE 2 Chemical reaction properties of the EVA material.

	A_0 (h^{-1})	E_a (kJ mol^{-1})	ΔH_R (kJ mol^{-1})
Reaction 1	$3.62\text{e}3^{53}$	64.8^{53}	-30.0^{54}
Reaction 2	$3.62\text{e}3^{53}$	64.8^{53}	-288.0^{54}
Reaction 3	$2.37\text{e}4^{55}$	104.7^{55}	-247.0^{56}
Reaction 4	$1.18\text{e}9^{31}$	107.5^{31}	-1076.5^{57}
Reaction 5	$1.18\text{e}9^{31}$	107.5^{31}	-1076.5^{57}

from both predictions and EL images, moisture diffuses from the free edges of the EVA layer towards the central area during aging, and they agree with each other very well. The captured EL images show the dark bands at the side area of EVA, which are not detected at the beginning (Figure 4A), and get thicker after 43 h (Figure 4B) and 81 h (Figure 4C). This trend that indicates the moisture ingress into the module over time⁵⁰ is well reproduced by the modeling method proposed in this work. To see the temperature effect on the diffusion phenomena, the contour plots of moisture diffusion and experimental EL images in the 65°C/85% RH and 45°C/85% RH damp heat tests are also compared and shown in Figures 5 and 6, respectively. Due to the temperature-dependent diffusion properties, the absolute humidity in these two cases differs from that in the 85°C/85% RH case. The diffusion phenomena are much slower in low-temperature conditions since the diffusion coefficients are smaller. It is clearly observed that the process for dark bands in the 65°C/85% RH case (see Figure 5) or 45°C/85% RH case (see Figure 6) to become thick is slower than that in the 85°C/85% RH damp heat case. Besides, it is worth noting that the absolute humidity in the 65°C/85% RH (see Figure 5) and 85°C/40% RH (see Figure 7) are almost equal to each other (1.25 kg/cm³ vs. 1.29 kg/cm³). However, due to the temperature difference, the diffusion phenomena are still different in these two cases.

The predicted time history evolution of moisture concentration at the positions with different distances away from the edge in the four different cases is shown in Figure 8. The moisture concentration at different positions increases over time as the diffusion phenomena proceed during the damp heat tests. Although the absolute humidity at the 65°C/85% RH and 85°C/40% RH cases are almost equal to each other, the diffusion time history demonstrates the significant difference, especially at the positions relatively far away from the free edge. As can be seen from Figure 8B,D, the trends of moisture concentration versus time curves at the position 10 mm far away from the edge in both cases are very similar, but as the distance increases from 20 to 70 mm away from the edge, the corresponding concentration versus time curve in the 85°C/40% RH case is obviously higher than that in the 65°C/85% RH case, indicating faster diffusion process in the former case that can be ascribed to its higher temperature.

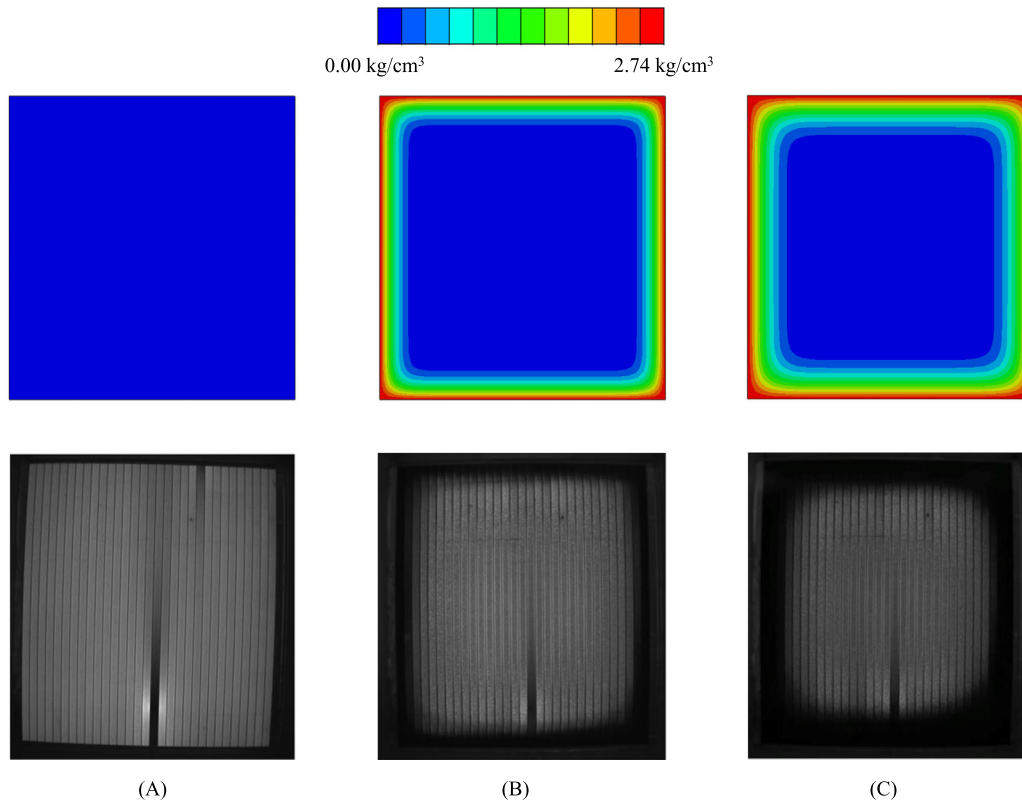


FIGURE 4 Comparison between the moisture diffusion contour plots obtained from simulation and the EL images taken from Reference 50 in the 85°C/85% RH damp heat test after (A) 0 h, (B) 43 h, and (C) 81 h.

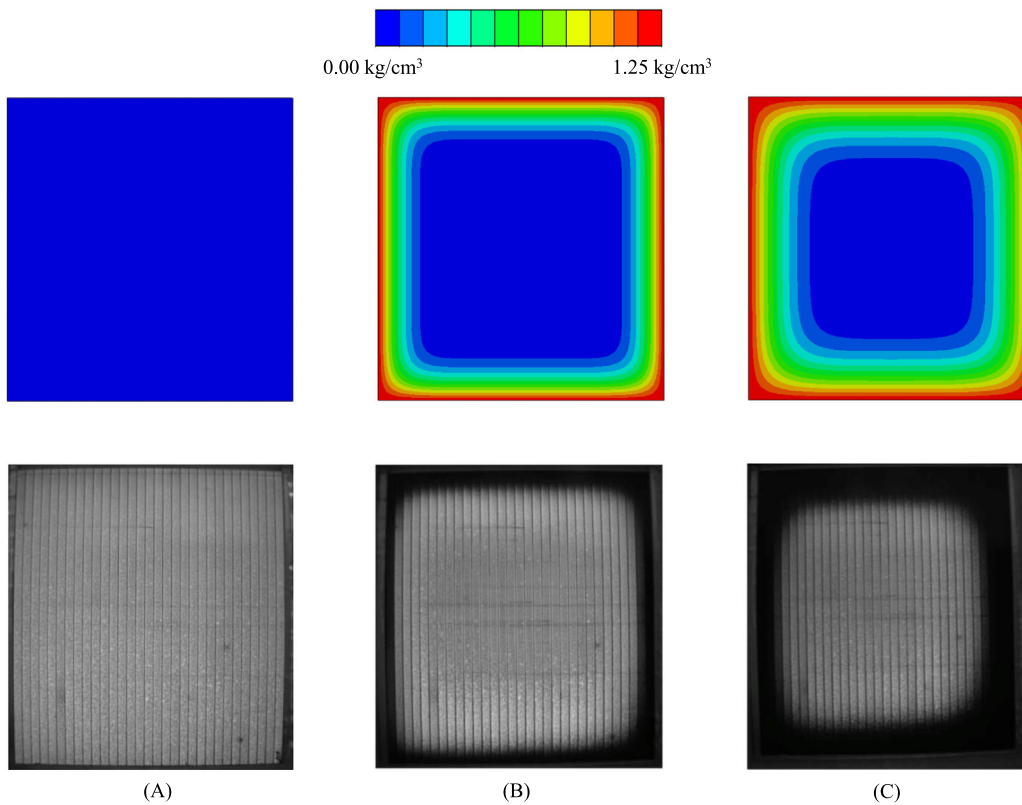


FIGURE 5 Comparison between the moisture diffusion contour plots obtained from simulation and the EL images taken from Reference 50 in the 65°C/85% RH damp heat test after (A) 0 h, (B) 130 h, and (C) 279 h.

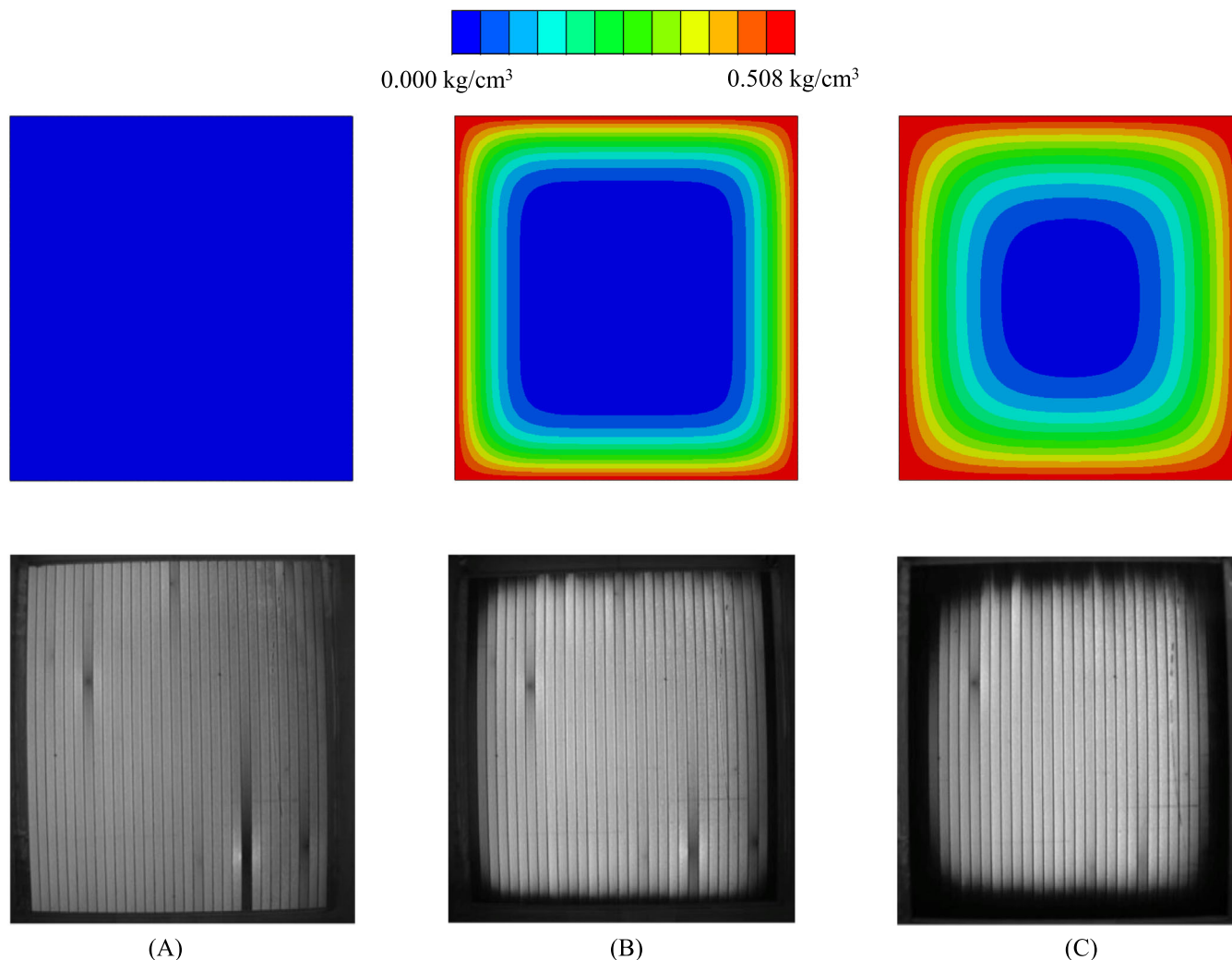


FIGURE 6 Comparison between the moisture diffusion contour plots obtained from simulation and the EL images taken from Reference 50 in the 45°C/85% RH damp heat test after (A) 0 h, (B) 321 h, and (C) 776 h.

The predicted spatial variation of moisture concentration in the four different damp heat cases after 200, 400, 600, and 800 h are shown in Figure 9. Moisture diffusion takes place from the free edges towards the center of the EVA layer and, as a result, moisture concentration at the central area increases over time for all the different hygrothermal conditions. For the 85°C/85% RH damp heat case, the concentration at the center of the module starts to increase after 400 h (see Figure 9B), and reaches around 0.5 kg/cm³ after 800 h (see Figure 9D), while for the 45°C/85% RH case, the moisture concentration at the center is still zero even after 800 h due to its low diffusivity. To further illustrate this point, it can also be observed that the spatial variation curves of moisture concentration in the 85°C/40% RH damp heat case are always above the red curves corresponding to the 65°C/85% RH damp heat case despite the approximate absolute humidity on the boundary.

The predicted chemical specie concentration ($[ET]$, $[R^*]$, $[U]$, and $[C_b]$) versus time in the 85°C/85% RH, 65°C/85% RH, and 45°C/85% RH damp heat tests are shown in Figure 10. The plots of $[ET]$ in Figure 10A indicate the overall degradation of the EVA layer, and the difference in the degradation process at the three tests can be ascribed to the influence of temperature on the kinetic rate of reaction k_1 . Higher temperature leads to the faster consumption of the $[ET]$ concentration. The produced concentration $[U]$ and $[C_b]$ (see Figure 10C,D) are much smaller than $[R^*]$ (see Figure 10B), being related to the secondary reaction type with very high activation energy. Due to the higher kinetic reaction rates resulting from higher temperature, the produced concentration $[R^*]$, $[U]$, and $[C_b]$ in the 85°C/85% RH damp heat case are all much higher than that produced in the other two cases, as shown in Figure 10B–D.

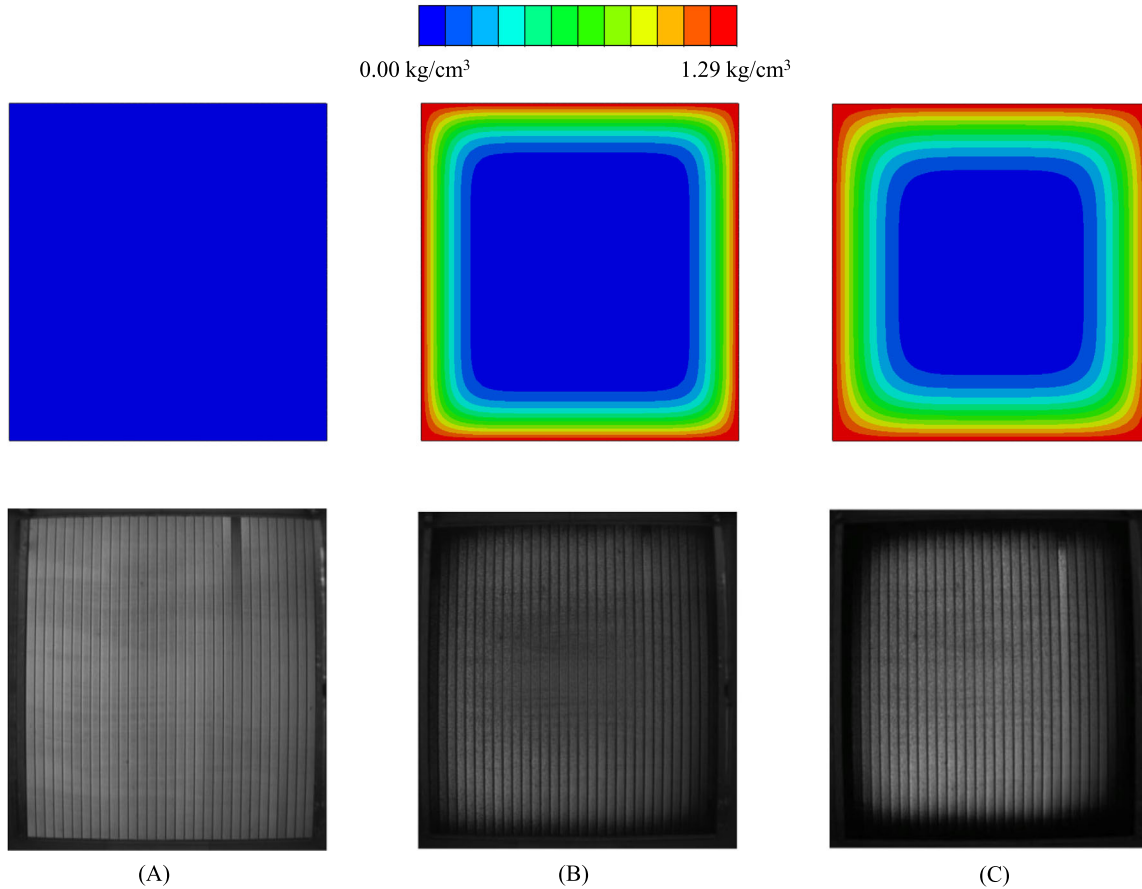


FIGURE 7 Comparison between the moisture diffusion contour plots obtained from simulation and the EL images taken from Reference 50 in the 85°C/40% RH damp heat test after (A) 0 h, (B)104, and (C) 187 h.

5.2 | Humidity freeze test

In the humidity freeze test, the photovoltaic modules are subjected to accelerated ageing under cyclic temperature boundary conditions. The cyclic temperature function is characterized by the following ramp

$$\theta^*(t) = \begin{cases} \frac{t}{t_1^*} \theta_1^* & 0 \leq t < t_1^*, \\ \theta_1^* & t_1^* \leq t < t_2^*, \\ \frac{t_3^* - t}{t_3^* - t_2^*} \theta_1^* & t_2^* \leq t < t_3^*, \\ \frac{t - t_3^*}{t_4^* - t_3^*} \theta_2^* & t_3^* \leq t < t_4^*, \\ \theta_2^* & t_4^* \leq t < t_5^*, \\ \frac{t_6^* - t}{t_6^* - t_5^*} \theta_2^* & t_5^* \leq t < t_6^*, \end{cases} \quad (60)$$

where $\theta_1^* = 85^\circ\text{C}$, $\theta_2^* = -40^\circ\text{C}$, and $t_1^* = 0.5$ h, $t_2^* = 1.5$ h, $t_3^* = 2.0$ h, $t_4^* = 2.5$ h, $t_5^* = 3.5$ h, $t_6^* = 4.0$ h, as shown in Figure 11. Compared with the damp heat case, the temperature inside the EVA layer cannot be assumed homogeneous and equal to the environmental temperature due to the cyclic variation of boundary temperature over time. Hence, the temperature must be treated as another independent variable that needs to be solved as the chemical reaction-diffusion system is temperature-dependent. Note that the thermo-mechanical problem is also coupled with the chemical system since internal heat is generated during the reaction processes. The mechanical and thermal properties of the glass and EVA layer are listed in Table 3, which are taken from.^{58,59}

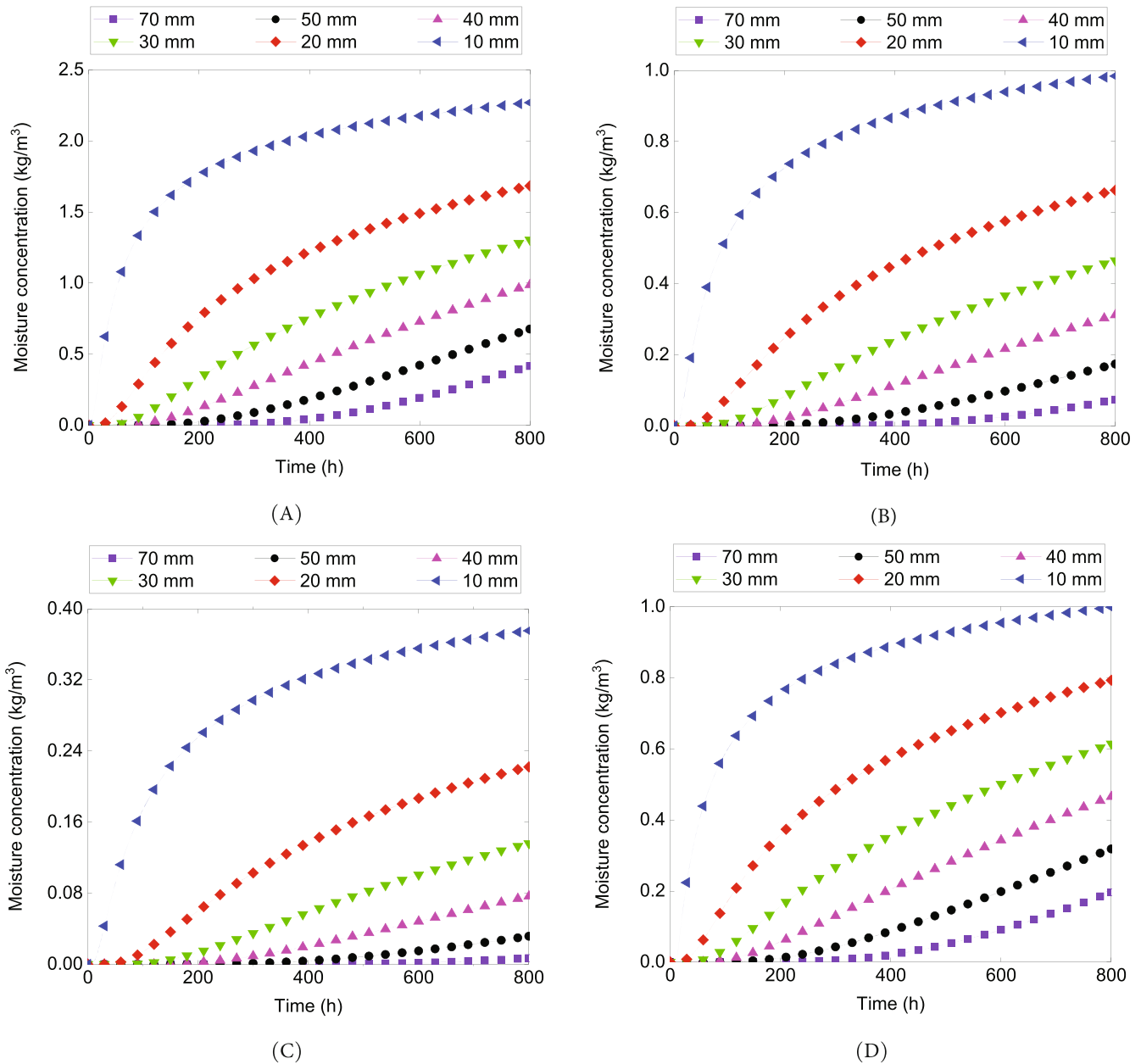


FIGURE 8 The plots of predicted moisture concentration versus time at the positions (70, 50, 40, 30, 20, and 10 mm away from the edge of EVA layer) in the (A) 85°C/85% RH damp heat case, (B) 65°C/85% RH damp heat case, (C) 45°C/85% RH damp heat case, and (D) 85°C/40% RH damp heat case.

The temperature inside the laminate strongly depends on the thermal properties of glass and EVA layers, and the spatial variation can be observed from the contour plots at time points A, B, C, and D during the first cycle, see Figure 12. The contour plots of the temperature inside the EVA layer at the four different time points during the first cycle are shown in Figure 13. At time point A, the temperature at the free edges of the EVA layer reaches 85°C and is kept constant for one hour until time point B. During this period, heat gradually diffuses into the central area of the EVA layer, leading to the spatial variation of temperature distribution, see Figure 13A,B. Also note that the lowest temperature inside the EVA layer at time point B reaches 8.99°C, which is higher than that at time point A due to the heat transfer. At time point C, the temperature of the boundary drops to -40°C, but the temperature in the central area of the EVA layer is still higher than 7°C, which results from the hysteresis effect of heat conduction. It is worth mentioning that this temporal and spatial temperature variation in the humidity freeze test leads to the difference in chemical reaction-diffusion from that in the damp heat test with the constant thermal condition.

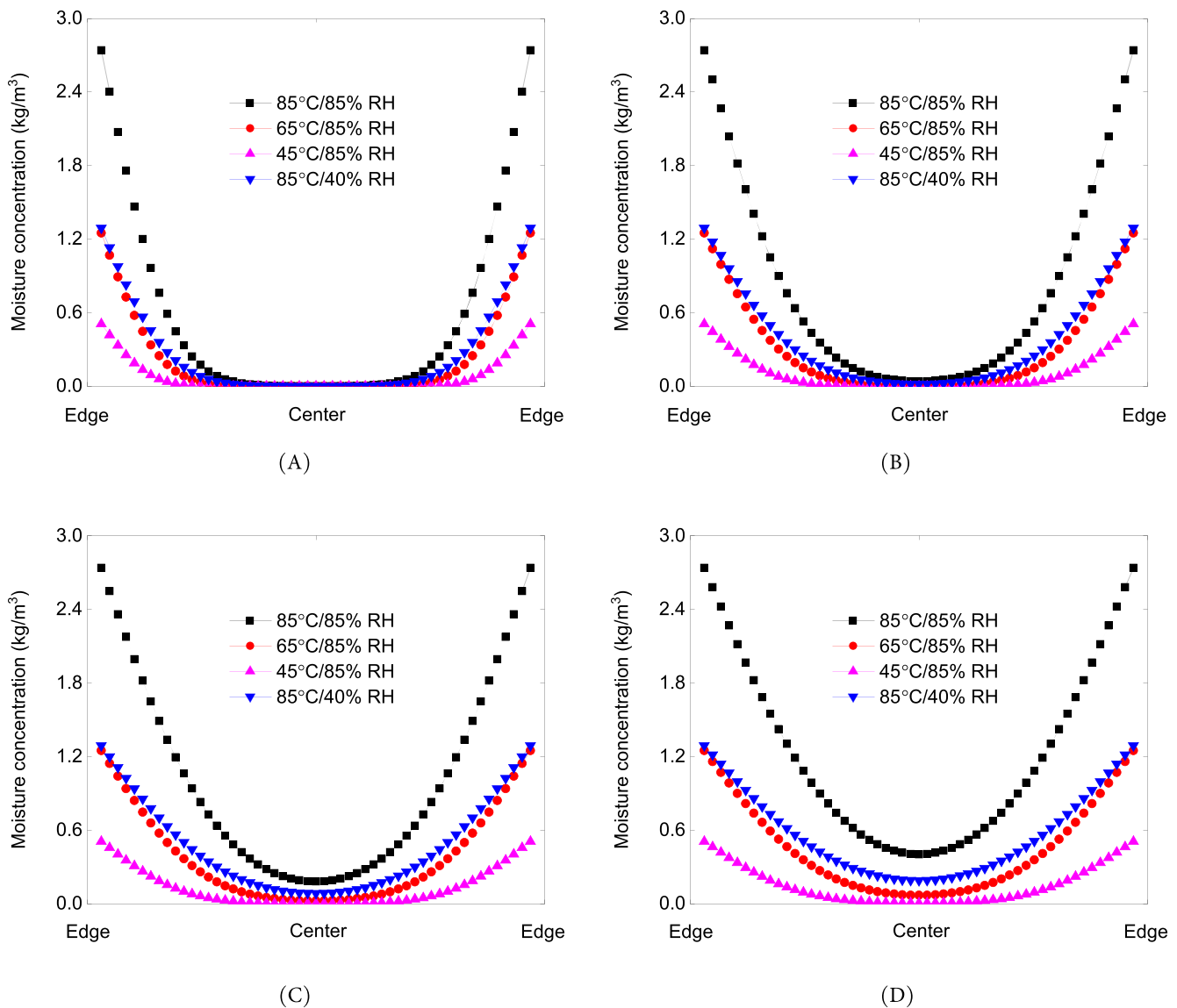


FIGURE 9 The spatial variation plots of predicted moisture concentration inside the EVA layer in the four different damp heat cases after (A) 200 h, (B) 400 h, (C) 600 h, and (D) 800 h.

The moisture diffusion contour plots after different time cycles during the humidity freeze test are shown in Figure 14. It can be seen that the moisture gradually diffuses into the center from the free edges, and the central area with zero moisture decreases over time during the simulation. The moisture concentration versus time curves at positions 10, 20, 30, 40, 50, and 70 mm far away from the free edges are shown in Figure 15. The moisture time history curves at all positions start to grow from zero and as time goes on, the water concentration at positions closer to the free edges definitely increase faster. To quantitatively see the influence of spatial temperature variation on the diffusion phenomena inside the EVA layer, the comparison of spatial concentration variation after 200 and 400 h between the 85°C/85% RH damp heat and the humidity freeze test are shown in Figure 16. It is clear that the amount of predicted moisture concentration across the EVA layer in the damp heat case is higher than that in the humidity freeze case at two different time points since the diffusion coefficient in the former case is higher arising from the constant higher temperature of 85°C. Note that the concentration across the EVA layer after 200 h in the damp heat case is even higher than that after 400 h in the humidity freeze case, which further demonstrates the significant influence of spatial temperature variation on the diffusion phenomena.

A position inside the EVA layer, which is 10 mm away from the edges, is selected to quantitatively evaluate the evolution of produced chemical specie concentration during the humidity freeze test with cyclic temperature boundary

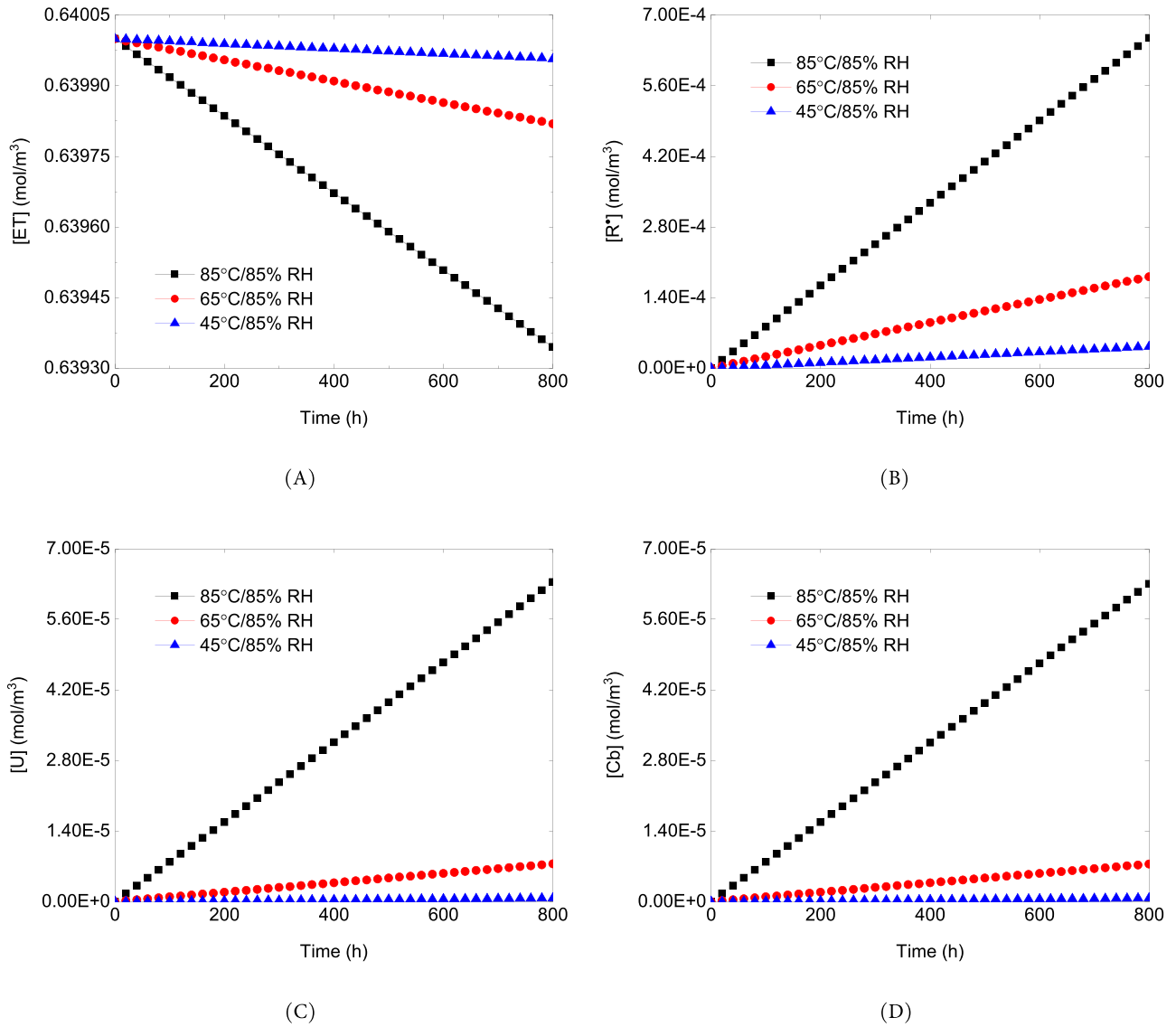


FIGURE 10 The predicted chemical specie concentration versus time in the 85°C/85% RH, 65°C/85% RH, and 45°C/85% RH damp heat tests.

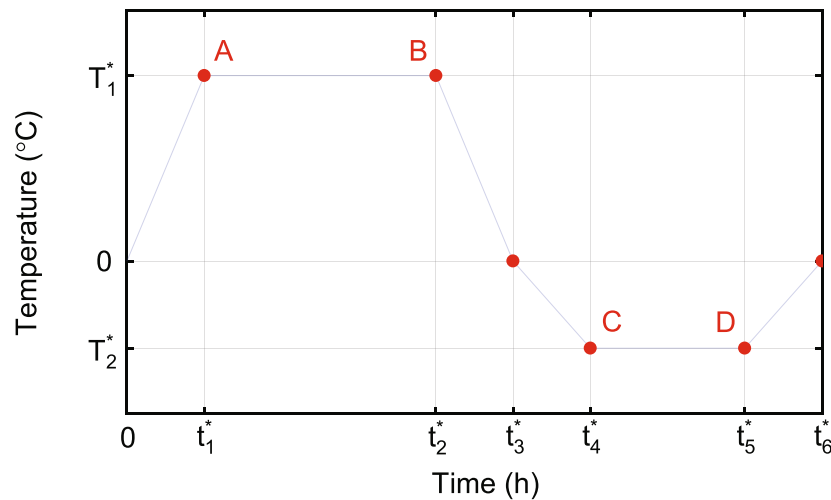


FIGURE 11 Temperature profile imposed on the PV modules during the humidity freeze test.

TABLE 3 Mechanical and thermal properties of the laminate.

	E (GPa)	ρ (kg/m ³)	α	c_p (J/kg K)	k_0 (W/m K)
EVA	0.05	950	1.6e-4	1400	0.34
Glass	73	2300	8e-6	500	0.8

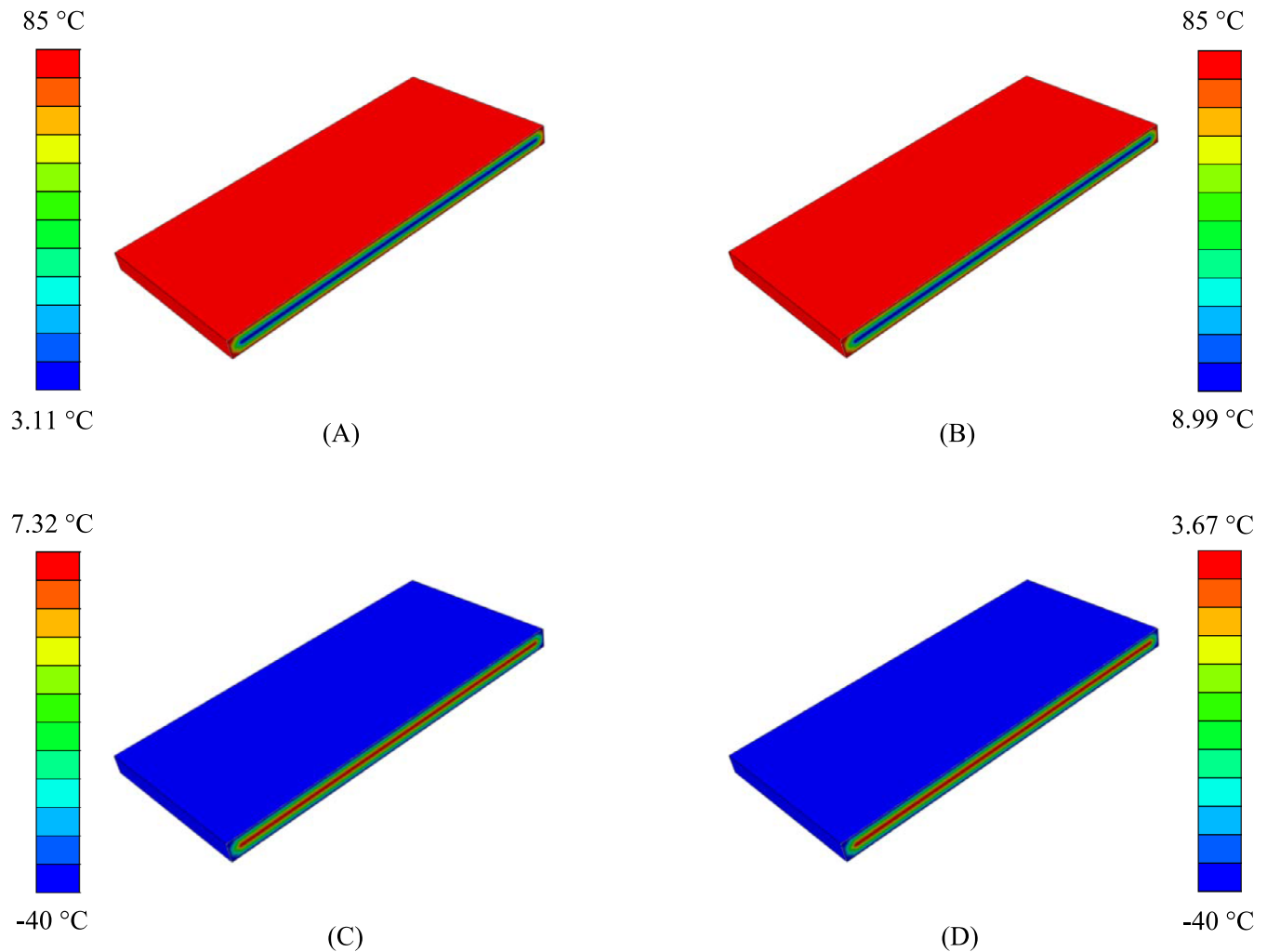


FIGURE 12 The predicted temperature distribution of the double glass laminate at four time points (A–D) during the first cycle of the humidity freeze test. (A) Time point A, (B) time point B, (C) time point C, (D) time point D.

condition, and the predicted ($[R^*]$, $[U]$, and $[C_b]$) versus time curves in the humidity freeze test are shown in Figure 17. It can be seen that the increasing amount of produced chemical species is 2–4 orders lower than that produced in the damp heat test with a constant temperature of 85°C. Given the boundary condition with a cyclic temperature profile, the temperature at this position is always lower than 85°C through the process, leading to the smaller kinetic rates of the chemical reaction system compared to the damp heat case.

6 | CONCLUDING REMARKS

This work presents a comprehensive methodology for the 3D modeling of the reaction-diffusion phenomena in PV modules within the coupled thermo-chemo-mechanical framework. The set of ordinary and partial differential equations was formulated for the description of the reaction-diffusion and thermo-mechanical problems. The governing

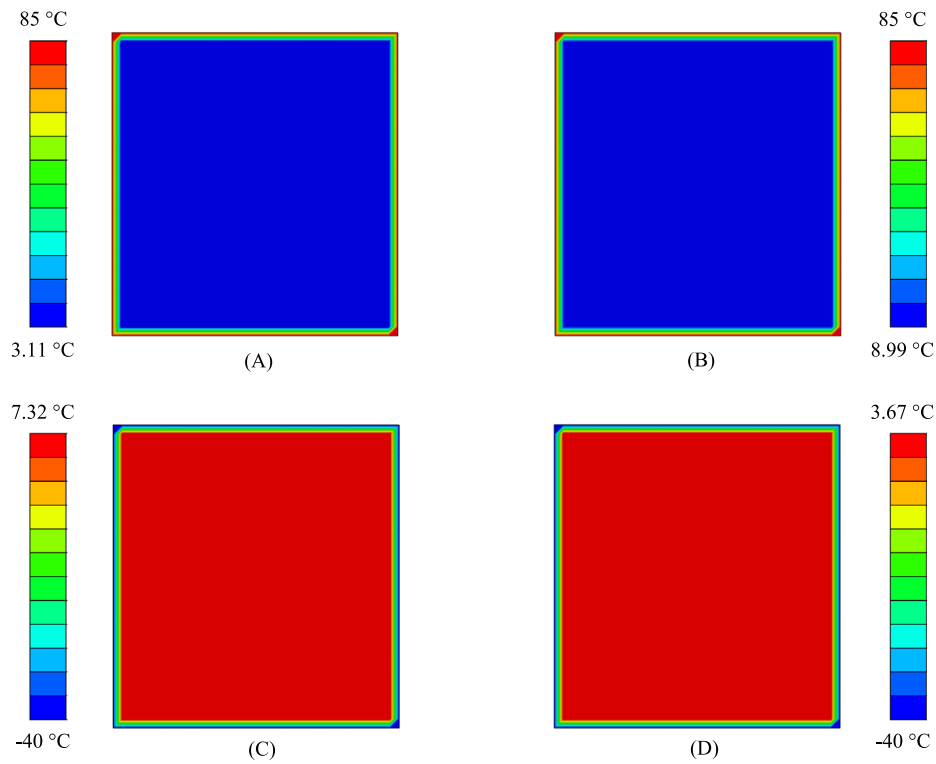


FIGURE 13 The predicted temperature distribution inside the EVA layer at four time points (A–D) during the first cycle of the humidity freeze test. (A) Time point A, (B) time point B, (C) time point C, (D) time point D.

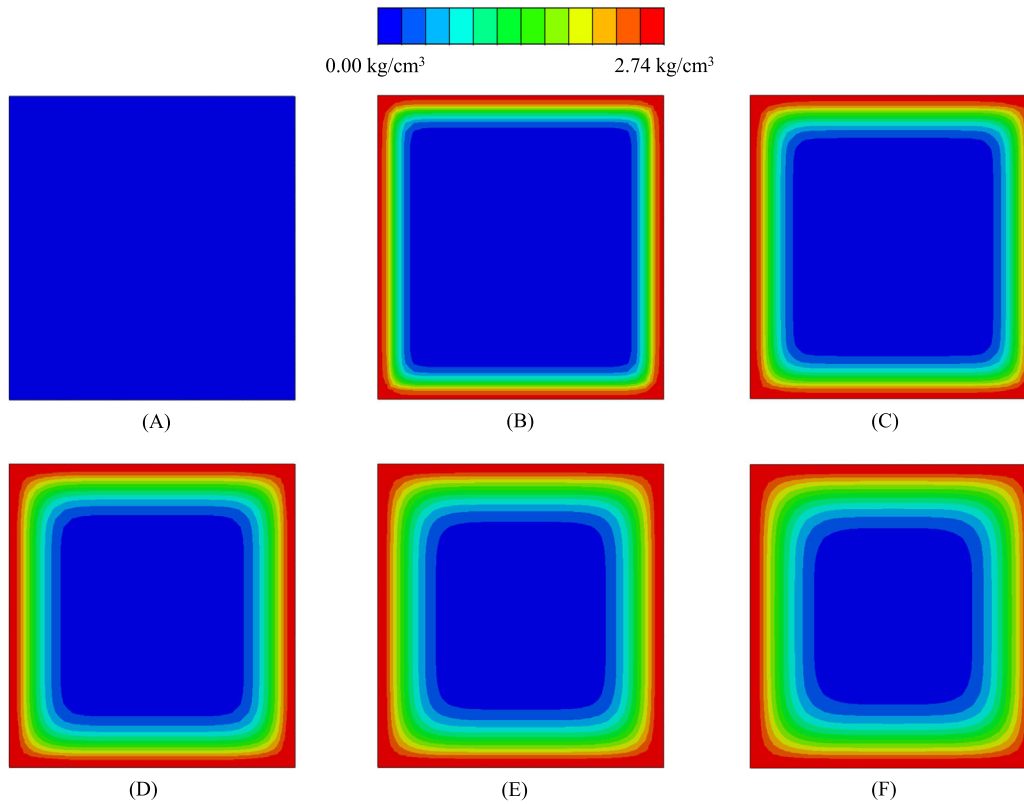


FIGURE 14 The predicted moisture distribution inside the EVA layer after different time cycles (A–F) during the humidity freeze test. (A) 0 cycle, (B) 50 cycle, (C) 100 cycle, (D) 150 cycle, (E) 200 cycle, (F) 250 cycle.

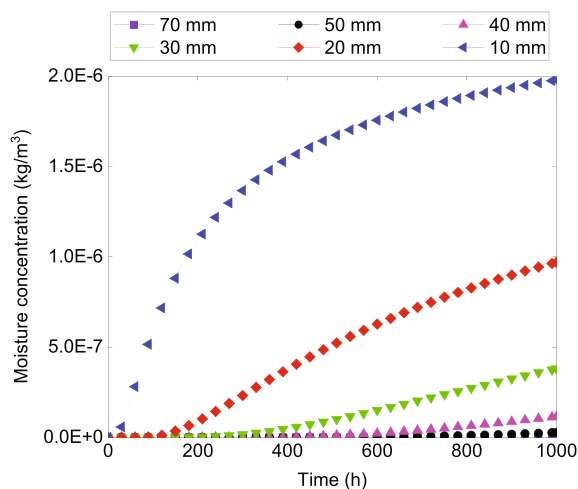


FIGURE 15 The predicted moisture distribution versus time curves at positions with different distances away from the free edges during the humidity freeze test.

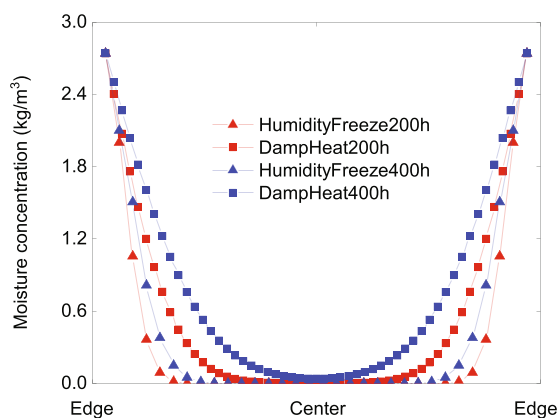


FIGURE 16 The comparison of predicted moisture distribution across the EVA layer after 200 and 400 h between the 85°C/85% RH damp heat and humidity freeze cases.

equations for the multifield coupled system are solved in a staggered scheme, and kinetic rates and coefficients in the reaction-diffusion analysis are updated based on the thermo-mechanical solution at each time increment. The proposed modeling framework is then applied to simulate the accelerated aging tests of PV modules, including the different damp heat tests with constant hygrothermal conditions and the humidity freeze test with cyclic temperature conditions. In the damp heat tests, the numerical predictions are compared with both the analytical solution and EL images at different stages obtained from experiments, and they agree with each other very well. Besides, the predictions of chemical degradation in the damp heat tests are also compared and significant differences in consumption rates of chemical species can be observed due to the temperature dependency of the reaction-diffusion system. The capability of the proposed method is further demonstrated through the simulation of the humidity freeze test, and taking into account the influence arising from the thermo-mechanical problem, the spatial and temporal variation of the diffusion and reaction species can be predicted as shown by the comparison with that of the damp heat simulation. The computational model has shown the potential to predict the degradation phenomena in the PV modules under different environmental conditions, which can be useful for the design of new protocols tailored for specific climate zones. The transport of chemical species and reaction-diffusion phenomena inside EVA are challenging to be predicted with enough accuracy due to the interplay between the thermal expansion and the environmental factors like oxygen and moisture, and has been the main focus of this study. To this aim, all the temperature dependency of the reaction-diffusion coefficients has been considered in the model, and a simplified numerical scheme has been proposed for the prediction of the temporal and spatial variation of

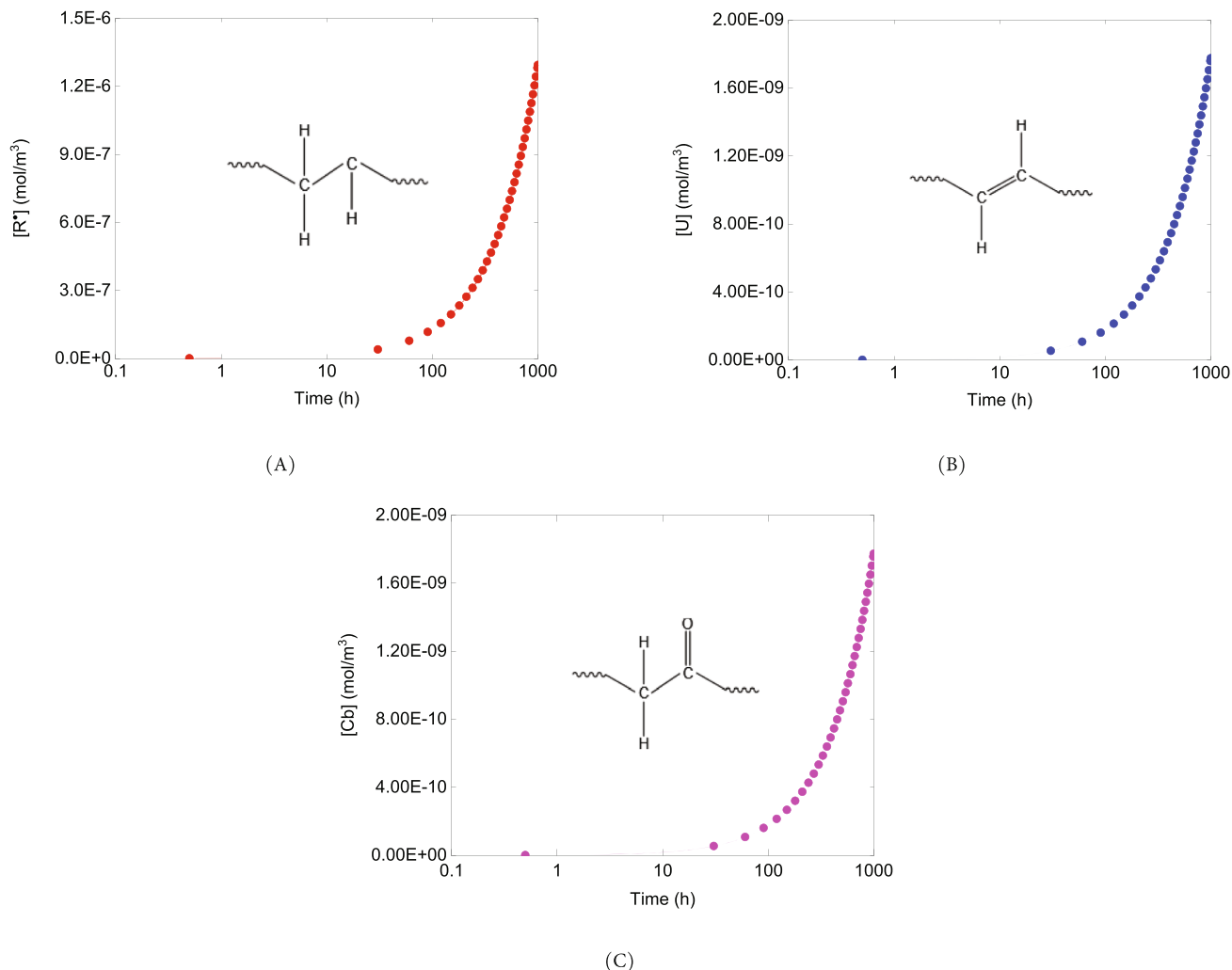


FIGURE 17 The predicted chemical specie concentration (A) $[R^*]$, (B) $[U]$, and (C) $[C_b]$ versus time in the humidity freeze case.

chemical species. With the increasing demands of PV modules, such kind of comprehensive modeling framework for the understanding of the complex degradation phenomena inside the EVA layers holds significance for quality assessment and prototyping.

ACKNOWLEDGMENTS

The authors acknowledge the funding received from the European Union's Horizon 2020 research and innovation program under the Marie Skłodowska-Curie grant agreement No. 861061; Project NEWFRAC.

M. Paggi would like to acknowledge the support provided by the Italian Ministry of University and Research to the project PRIN2017 "XFAST-SIMS: Extra fast and accurate simulation of complex structural systems", GA 20173C478N.

J. Reinoso is grateful to the Consejería de Economía y Conocimiento of the Junta de Andalucía (Spain) for financial support under the contract US-1265577-Programa Operativo FEDER Andalucía 2014–2020, and the support of the Spanish Ministerio de Ciencia, Innovación y Universidades the under the grant PID2019-109723GB-I00 and Consejería de Economía y Conocimiento of the Junta de Andalucía (Spain) under the grant P2-00595. J. Reinoso is also grateful to the support of Ministerio de Ciencia e Innovacion of Spain under the grant TED2021-131649B-100.

CONFLICT OF INTEREST STATEMENT

The authors declare that they have no known competing financial interests or personal relationships that could have appeared to influence the work reported in this paper.

DATA AVAILABILITY STATEMENT

The data that support the findings of this study are available upon request.

ORCID

Zeng Liu  <https://orcid.org/0000-0002-7244-6947>

REFERENCES

1. Delgado-Sanchez J-M, Sanchez-Cortezon E, Lopez-Lopez C, Aninat R, Alba MD. Failure mode and effect analysis of a large scale thin-film CIGS photovoltaic module. *Eng Fail Anal.* 2017;76:55-60.
2. Liu Z, Reinoso J, Paggi M. A humidity dose-CZM formulation to simulate new end-of-life recycling methods for photovoltaic laminates. *Eng Fract Mech.* 2022;259:108125.
3. Deng G, Ma W, Peng Y, Wang S, Yao S, Peng S. Experimental study on laminated glass responses of high-speed trains subject to windblown sand particles loading. *Constr Build Mater.* 2021;300:124332.
4. Theelen M, Beyeler K, Steijvers H, Barreau N. Stability of CIGS solar cells under illumination with damp heat and dry heat: a comparison. *Sol Energy Mater Sol Cells.* 2017;166:262-268.
5. Verri M, Porro M, Sacco R, Salsa S. Solution map analysis of a multiscale drift-diffusion model for organic solar cells. *Comput Methods Appl Mech Eng.* 2018;331:281-308.
6. de Falco C, Porro M, Sacco R, Verri M. Multiscale modeling and simulation of organic solar cells. *Comput Methods Appl Mech Eng.* 2012;245:102-116.
7. Liu Z, Reinoso J, Paggi M. Hygro-thermo-mechanical modeling of thin-walled photovoltaic laminates with polymeric interfaces. *J Mech Phys Solids.* 2022;169:105056.
8. Segbefia OK, Imenes AG, Saetre TO. Moisture ingress in photovoltaic modules: a review. *Sol Energy.* 2021;224:889-906.
9. Theelen M, Daume F. Stability of Cu (In, Ga) Se₂ solar cells: a literature review. *Sol Energy.* 2016;133:586-627.
10. Lee TD, Ebone AU. A review of thin film solar cell technologies and challenges. *Renew Sustain Energy Rev.* 2017;70:1286-1297.
11. Sol EM, de la Casa J, Romero-Fiances I, Silva JP, Nofuentes G. A study on the degradation rates and the linearity of the performance decline of various thin film PV technologies. *Sol Energy.* 2019;188:813-824.
12. Kumar S, Meena R, Gupta R. Imaging and micro-structural characterization of moisture induced degradation in crystalline silicon photovoltaic modules. *Sol Energy.* 2019;194:903-912.
13. Han H, Yan H, Wang X, et al. Analysis of the degradation of encapsulant materials used in photovoltaic modules exposed to different climates in China. *Sol Energy.* 2019;194:177-188.
14. Marwaha S, Ghosh K. Analytical modeling of diffusion of moisture in silicon photovoltaic module under damp heat testing condition. *Silicon.* 2022;14(9):4757-4766.
15. Wisniewski D, Lv R, Nair SV, Jaubert J-N, Xu T, Ruda HE. Measurement and modelling of water ingress into double-glass photovoltaic modules. *Prog Photovolt Res Appl.* 2019;27(2):144-151.
16. Dadaniya A, Datta NV. Water diffusion simulation in photovoltaic module based on the characterization of encapsulant material using in-situ gravimetric technique. *Sol Energy Mater Sol Cells.* 2019;201:110063.
17. Paggi M, Corrado M, Rodriguez MA. A multi-physics and multi-scale numerical approach to microcracking and power-loss in photovoltaic modules. *Compos Struct.* 2013;95:630-638.
18. Gagliardi M, Lenarda P, Paggi M. A reaction-diffusion formulation to simulate EVA polymer degradation in environmental and accelerated ageing conditions. *Sol Energy Mater Sol Cells.* 2017;164:93-106.
19. Gawin D, Pesavento F, Schrefler B. Modelling of hygro-thermal behaviour of concrete at high temperature with thermo-chemical and mechanical material degradation. *Comput Methods Appl Mech Eng.* 2003;192(13-14):1731-1771.
20. Kodali HK, Ganapathysubramanian B. A computational framework to investigate charge transport in heterogeneous organic photovoltaic devices. *Comput Methods Appl Mech Eng.* 2012;247:113-129.
21. Cao T, Sanavia L, Schrefler B. A thermo-hydro-mechanical model for multiphase geomaterials in dynamics with application to strain localization simulation. *Int J Numer Methods Eng.* 2016;107(4):312-337.
22. Ottersböck B, Oreski G, Pinter G. How to accelerate natural weathering of polymeric photovoltaic backsheets—a comparison with standardized artificial aging. *Sol Energy Mater Sol Cells.* 2022;244:111819.
23. Thornton P, Moffitt SL, Schelhas LT, Dauskardt RH. Dependence of adhesion on degradation mechanisms of ethylene co-vinyl acetate encapsulants over the lifetime of photovoltaic modules. *Sol Energy Mater Sol Cells.* 2022;244:111818.
24. Iqbal N, Colvin DJ, Schneller EJ, et al. Characterization of front contact degradation in monocrystalline and multicrystalline silicon photovoltaic modules following damp heat exposure. *Sol Energy Mater Sol Cells.* 2022;235:111468.
25. Lelièvre J-F, Couderc R, Pinochet N, et al. Desert label development for improved reliability and durability of photovoltaic modules in harsh desert conditions. *Sol Energy Mater Sol Cells.* 2022;236:111508.
26. Allen NS, Edge M, Rodriguez M, Liauw CM, Fontan E. Aspects of the thermal oxidation, yellowing and stabilisation of ethylene vinyl acetate copolymer. *Polym Degrad Stab.* 2000;71(1):1-14.
27. Steffen R, Akraa MA-H, Röder B. Kinetics of degradation-induced photoluminescence in ethylene-vinyl-acetate as used in photovoltaic modules. *Sol Energy Mater Sol Cells.* 2020;206:110294.
28. Kempe MD. Modeling of rates of moisture ingress into photovoltaic modules. *Sol Energy Mater Sol Cells.* 2006;90(16):2720-2738.

29. Marais S, Hirata Y, Langevin D, Chappey C, Nguyen TQ, Metayer M. Permeation and sorption of water and gases through EVA copolymers films. *Mater Res Innov.* 2002;6(2):79-88.
30. Pern F. Factors that affect the EVA encapsulant discoloration rate upon accelerated exposure. *Sol Energy Mater Sol Cells.* 1996;41:587-615.
31. Rimez B, Rahier H, van Assche G, Artoos T, Biesemans M, van Mele B. The thermal degradation of poly (vinyl acetate) and poly (ethylene-co-vinyl acetate), Part I: experimental study of the degradation mechanism. *Polym Degrad Stab.* 2008;93(4):800-810.
32. Hülsmann P, Weiss K-A. Simulation of water ingress into PV-modules: IEC-testing versus outdoor exposure. *Sol Energy.* 2015;115:347-353.
33. Lenarda P, Paggi P. A geometrical multi-scale numerical method for coupled hygro-thermo-mechanical problems in photovoltaic laminates. *Comput Mech.* 2016;57(6):947-963. doi:10.1007/s00466-016-1271-5
34. Serra E, Bonaldi M. A finite element formulation for thermoelastic damping analysis. *Int J Numer Methods Eng.* 2009;78(6):671-691.
35. Kumar PKAV, Dean A, Reinoso J, Paggi M. Thermo-elastic solid shell formulation with phase field fracture for thin-walled FGMS. *Thin-Walled Struct.* 2022;179:109535.
36. Kumar PKAV, Dean A, Reinoso J, Paggi M. Nonlinear thermo-elastic phase-field fracture of thin-walled structures relying on solid shell concepts. *Comput Methods Appl Mech Eng.* 2022;396:115096.
37. Kumar PKAV, Dean A, Sahraee S, Reinoso J, Paggi M. Non-linear thermoelastic analysis of thin-walled structures with cohesive-like interfaces relying on the solid shell concept. *Finite Elem Anal des.* 2022;202:103696.
38. Kholodovych V, Welsh WJ. Thermal-oxidative stability and degradation of polymers. *Physical Properties of Polymers Handbook.* Springer; 2007:927-938.
39. Kodera Y, McCoy BJ. Distribution kinetics of radical mechanisms: reversible polymer decomposition. *AIChE J.* 1997;43(12):3205-3214.
40. Liang R, Chung S, Clayton A, et al. Photothermal degradation of ethylene/vinylacetate copolymer. *Polymer Alloys III.* Springer; 1983:267-278.
41. Francois-Heude A, Richaud E, Desnoux E, Colin X. Influence of temperature, UV-light wavelength and intensity on polypropylene photothermal oxidation. *Polym Degrad Stab.* 2014;100:10-20.
42. Klemchuk P, Ezrin M, Lavigne G, Holley W, Galica J, Agro S. Investigation of the degradation and stabilization of EVA-based encapsulant in field-aged solar energy modules. *Polym Degrad Stab.* 1997;55(3):347-365.
43. Pern F. Ethylene-vinyl acetate (EVA) encapsulants for photovoltaic modules: degradation and discoloration mechanisms and formulation modifications for improved photostability. *Die Angew Makromolekul Chemie: Appl Macromolecul Chem Phy.* 1997;252(1):195-216.
44. Wiles D. Photostabilization of macromolecules by excited state quenching. *Macromolecular Chemistry.* Elsevier; 1979:291-297.
45. Wang H. *Comprehensive Organic Name Reactions.* Wiley; 2010.
46. Yang R, Christensen P, Egerton T, White J. Degradation products formed during UV exposure of polyethylene-zno nano-composites. *Polym Degrad Stab.* 2010;95(9):1533-1541.
47. Ruban L, Sychugova O, Kolesnikova N, Zaikov G. Kinetic features of the nonisothermal oxidative degradation of ethylene vinyl acetate copolymers. *J Appl Polym Sci.* 2004;91(3):1958-1961.
48. Vahdat N, Sullivan VD. Estimation of permeation rate of chemicals through elastometric materials. *J Appl Polym Sci.* 2001;79(7):1265-1272.
49. Liu Z, Reinoso J, Paggi M. Phase field modeling of brittle fracture in large-deformation solid shells with the efficient quasi-newton solution and global-local approach. *Comput Methods Appl Mech Eng.* 2022;399:115410.
50. Han C. Analysis of moisture-induced degradation of thin-film photovoltaic module. *Sol Energy Mater Sol Cells.* 2020;210:110488.
51. Crank J. *The Mathematics of Diffusion.* Oxford University Press; 1979.
52. Hernández H, Massart T, Peerlings R, Geers M. A stabilization technique for coupled convection-diffusion-reaction equations. *Int J Numer Methods Eng.* 2018;116(1):43-65.
53. Korcek S, Chenier J, Howard J, Ingold K. Absolute rate constants for hydrocarbon autoxidation. XXI. Activation energies for propagation and the correlation of propagation rate constants with carbon-hydrogen bond strengths. *Can J Chem.* 1972;50(14):2285-2297.
54. Bockhorn H, Hornung A, Hornung U, Schawaller D. Kinetic study on the thermal degradation of polypropylene and polyethylene. *J Anal Appl Pyrolysis.* 1999;48(2):93-109.
55. Karpukhin ON, Slobodetskaya EM. Kinetics of the photochemical oxidation of polyolefins. *Russ Chem Rev.* 1973;42(3):173.
56. Russell GA. Deuterium-isotope effects in the autoxidation of aralkyl hydrocarbons. Mechanism of the interaction of peroxy radicals1. *J Am Chem Soc.* 1957;79(14):3871-3877.
57. Speight JG. *Lange's Handbook of Chemistry.* McGraw-Hill Education; 2005.
58. Eitner U, Kajari-Schröder S, Köntges M, Altenbach H. Thermal stress and strain of solar cells in photovoltaic modules. *Shell-like Structures.* Springer; 2011:453-468.
59. Paggi M, Kajari-Schröder S, Eitner U. Thermomechanical deformations in photovoltaic laminates. *J Strain Anal Eng des.* 2011;46(8):772-782.

How to cite this article: Liu Z, Lenarda P, Reinoso J, Paggi M. A multifield coupled thermo-chemo-mechanical theory for the reaction-diffusion modeling in photovoltaics. *Int J Numer Methods Eng.* 2023;1-26. doi: 10.1002/nme.7233